The Astrophysical Journal, 656:1075–1091, 2007 February 20
© 2007. The American Astronomical Society. All rights reserved. Printed in U.S.A.

REVEALING THE NATURE OF ALGOL DISKS THROUGH OPTICAL AND UV SPECTROSCOPY, SYNTHETIC SPECTRA, AND TOMOGRAPHY OF TT HYDRAE

Brendan Miller, Ján Budaj,[1,2] and Mercedes Richards[3]
Department of Astronomy and Astrophysics, Pennsylvania State University, University Park, PA;
bmiller@astro.psu.edu, budaj@as.arizona.edu, mrichards@astro.psu.edu

Pavel Koubský[3]
Astronomical Institute, Academy of Sciences of the Czech Republic, Ondřejov, Czech Republic; koubsky@sunstel.asu.cas.cz

and

Geraldine J. Peters[3]
Space Sciences Center, University of Southern California, Los Angeles, CA; gjpeters@mucen.usc.edu
Received 2006 April 10; accepted 2006 October 29

ABSTRACT

We have developed a systematic procedure to study the disks in Algol-type binaries using spectroscopic analysis, synthetic spectra, and tomography. We analyzed 119 Hα spectra of TT Hya, an Algol-type eclipsing interacting binary, collected from 1985 to 2001. The new radial velocities enabled us to derive reliable orbital elements, including a small nonzero eccentricity, and to improve the accuracy of the absolute dimensions of the system. High-resolution *IUE* spectra were also analyzed to study the formation of the UV lines and continuum. Synthetic spectra of the iron curtain using our new SHELLSPEC program enabled us to derive a characteristic disk temperature of 7000 K. We have demonstrated that the UV emission lines seen during total primary eclipse cannot originate from the accretion disk but most likely arise from a hotter disk-stream interaction region. The synthetic spectra of the stars, disk, and stream allowed us to derive a mass transfer rate $\geq 2\times10^{-10}$ $M_\odot$ yr^{-1}. Doppler tomography of the observed Hα profiles revealed a distinct accretion disk. The difference spectra produced by subtracting the synthetic spectra of the stars resulted in an image of the disk, which virtually disappeared once the composite synthetic spectra of the stars and disk were used to calculate the difference spectra. An intensity enhancement of the resulting tomogram revealed images of the gas stream and an emission arc. We successfully modeled the gas stream using SHELLSPEC and associated the emission arc with an asymmetry in the accretion disk.

Subject headings: accretion, accretion disks — binaries: eclipsing — novae, cataclysmic variables — radiative transfer — stars: individual (TT Hydrae)

Online material: color figures

1. INTRODUCTION

The Algol-type binaries are interacting systems consisting of a hot, usually more massive, main-sequence star and a cool giant or subgiant that fills its Roche lobe. While these binaries should be randomly oriented, more eclipsing systems have been discovered since these systems are more easily detected through their distinct light curves. By convention, the hotter star (associated with the deeper minimum) is referred to as the "primary" and the cooler star as the "secondary." The secondary is losing mass to its companion, and we observe circumstellar material in the form of a gas stream, an accretion annulus, or an accretion disk. The most recent paper that summarizes our current knowledge of the Algols is the work by Richards & Albright (1999). Some recent progress in the field includes the detection and study of the pulsation of primary stars (Lehmann & Mkrtichian 2004; Mkrtichian et al. 2005), evidence of the superhump phenomenon in the radio power spectrum of β Per (Retter et al. 2005), the calculation and modeling of synthetic spectra (Barai et al. 2004; Budaj et al. 2005, hereafter BRM05; Korčaková et al. 2005), far-ultraviolet (FUV) and X-ray studies (Chung et al. 2004; Peters & Polidan 2004), Doppler tomography of the accretion structures (Richards 2004; Barai et al. 2004), eclipse mapping (Pavlovski et al. 2006), new orbits and fundamental parameters of eclipsing systems (Milone et al. 2005), hydrodynamic simulations of the mass transfer process (Richards & Ratliff 1998; Nazarenko et al. 2005), a survey of Hα mass transfer structures (Vesper et al. 2001), and a study of the evolution of Algol systems (Maxted & Hilditch 1996).

TT Hydrae (HD 97528, HIP 54807, SAO 179648, $V = 7.27$ mag, $\alpha = 11^{\rm h}13^{\rm m}$, $\delta = -26^\circ28'$) is a long-period ($P_{\rm orb} = 6.95$ days) Algol-type eclipsing binary system that consists of a hotter B9.5 V main-sequence primary and a cooler evolved K1 III–IV secondary star that fills its Roche lobe. Plavec & Polidan (1976) found evidence of mass transfer in the form of an accretion disk surrounding the primary. Kulkarni & Abhyankar (1980) obtained *UBV* photometric observations and elements of the system. These observations were reexamined by Etzel (1988), who found from photometry, spectrophotometry, and spectroscopy that $T_{\rm eff} =$ 9800 K, $v \sin i = 168 \pm 5$ km s^{-1} for the primary, and $T_{\rm eff} = 4670$–4850 K for the secondary, photometric mass ratio $q = 0.184$, and $i = 84.415 \pm 0.042$. He also estimated a distance of 193 pc to the binary. Eaton & Henry (1992) estimated $v \sin i = 43 \pm 3$ km s^{-1}

[1] Astronomical Institute, Tatranská Lomnica, Slovak Republic.
[2] Current address: Department of Astronomy, University of Arizona, Tucson, AZ.
[3] Visiting Astronomer, Kitt Peak National Observatory, National Optical Astronomy Observatory. NOAO is operated by AURA, Inc. under contract to the NSF.

TABLE 1
SUMMARY OF THE OPTICAL OBSERVATIONS OF TT HYA

Dates	Observatory	Chip	Resolution	Data	Observers
1956 Apr–1977 Apr	Mount Wilson/Lick	...	11–20 Å mm^{-1}	27	Popper (radial velocities only)
1985 Feb–1991 Mar	KPNO	TI3	0.221 Å pixel^{-1}	57	Peters
1994 Apr–1994 Apr	KPNO	T1KA	0.166 Å pixel^{-1}	4	Peters
1994 Jun–1994 Dec	KPNO	T1KA	0.166 Å pixel^{-1}	23	Richards, Albright, Koubský
1996 Feb–1997 Jun	KPNO	F3KB	0.105 Å pixel^{-1}	24	Richards & Koubský
1999 Jan–2001 Jan	KPNO	F3KB	0.105 Å pixel^{-1}	11	Peters

for the secondary and suggested that the mass ratio, as well as the mass of the primary, should be slightly higher than those found by Etzel (1988) if the secondary fills its Roche lobe.

Plavec (1988) studied the *International Ultraviolet Explorer* (*IUE*) spectra and concluded from the presence of Fe II absorption lines that the vertical dimension of the accretion disk is significant and is at least comparable to the diameter of the primary. He estimated a distance to the system of 194 pc and pointed out that the presence of superionized emission lines of Si IV, C IV, and N V poses a question about the ionization source. Peters (1989) estimated from the eclipses of the Hα emission region that a fairly symmetrical disk fills up to 95% of the Roche lobe radius. Moreover, she argued that the disk must be rather flat with the vertical dimension comparable to or less than the diameter of the primary. The depth of the Hα core was found to be strongly variable with phase and was deepest shortly before and after the primary eclipse, a feature also observed in other Algols (e.g., Richards 1993).

Sahade & Cesco (1946) determined the orbital parameters of the primary and identified a highly eccentric orbit from the Ca II K and H lines. Miller & McNamara (1963) measured a few radial velocities of the primary and secondary. Popper (1989) measured radial velocities of the primary and secondary and found that the radial velocities of the secondary were consistent with a circular orbit ($K = 132$ km s^{-1}), but this was not true in the case of the primary. The radial velocities of the primary suggested a mass ratio of about $q = 0.26$, which is not in very good agreement with the photometric value. Van Hamme & Wilson (1993) reanalyzed the light and velocity curves separately and simultaneously and used a physical model to obtain the following parameters: separation $a = 22.63 \pm 0.12\ R_\odot$, effective temperature of the primary $T_1 = 9800$ K, secondary $T_2 = 4361$ K, radius of the primary $R_1 = 1.95\ R_\odot$, secondary $R_2 = 5.87\ R_\odot$, mass of the primary $M_1 = 2.63\ M_\odot$, secondary $M_2 = 0.59\ M_\odot$, and mass ratio $q = 0.2261 \pm 0.0008$. Vivekananda & Sarma (1994) reanalyzed the original Kulkarni & Abhyankar (1980) data using the Wilson-Devinney code (Wilson & Devinney 1971) and obtained a photometric mass ratio of $q = 0.2963$, which is very close to the spectroscopic value derived by Popper (1989).

Albright & Richards (1996) obtained the first Doppler tomogram of TT Hya and produced an indirect image of the accretion disk. Peters & Polidan (1998) observed redshifted absorption in N I and N II lines in their FUV spectra at the phase 0.95 and interpreted it as evidence of the gas stream; consequently, they were able to infer that the rate of inflow was greater than $10^{-12}\ M_\odot$ yr^{-1}. Richards & Albright (1999) studied the Hα difference profiles and properties of the accretion region and placed TT Hya in the context of other Algol binaries. Most recently, BRM05 produced synthetic Hα spectra, compared the synthetic and observed profiles, determined the physical properties of the disk, and found evidence of the gas stream in these profiles. They also suggested the presence of an additional circumstellar structure between the C1 and C2 Lagrangian surfaces, in the vicinity of the secondary star, to explain the strong Hα line cores and other effects.

In this work we have reexamined the earlier conclusions by analyzing previously unpublished Hα spectra of TT Hya. These observations are described in § 2. In § 3 we describe the study of the optical spectra, the redetermination of orbital elements and absolute dimensions of the system from new velocity curves, and the study of the radial velocities of the profiles. In addition, synthetic Hα spectra were calculated, and a variety of difference spectra were determined by subtracting synthetic spectra from the observed Hα profiles. In § 4 archival high-resolution ultraviolet spectra were used to provide a consistent model for the accretion structures in TT Hya. In § 5 we show how Doppler tomography was used to study the accretion structures in the binary and as a tool to examine the quality of the fits between the observed and synthetic spectra. Finally, the conclusions are presented in § 6.

2. THE OBSERVATIONS

The 119 optical spectra described in this work were obtained by various observers from 1985 to 2001 (see Table 1). All spectra were collected with the 0.9 m coudé feed telescope at Kitt Peak National Observatory (KPNO). These spectra have a resolution of 0.34 Å and dispersion at Hα of $\sim$7.0 Å mm^{-1}. The data can be separated roughly into two major groups: 1985 February–1991 March (group 1) and 1994 April–2001 January (group 2). In addition, we used the original 27 radial velocity measurements of Popper (1989) based on spectra collected from 1956 to 1977 at Mount Wilson and Lick Observatories at a resolution of 11–20 Å mm^{-1} (see Table 1). The UT dates, HJD, and epochs of the KPNO data are listed in columns (1)–(3) of Table 2.

The ultraviolet spectra of TT Hya were obtained with the *IUE* telescope from 1980 to 1992. The short-wavelength range (1150–1950 Å) was covered by the SWP camera, while the long-wavelength range (1900–3200 Å) was covered by the LWP and LWR cameras (Kondo 1987). The high-resolution *IUE* spectra have a resolution of 0.1–0.3 Å or $R = 10{,}000$. Only the high-resolution spectra are studied here since the low-resolution spectra are not suitable for radial velocity studies. Moreover, these high-resolution *IUE* spectra are similar in resolution to the optical spectra. Six long-wavelength (LWP and LWR) spectra and 11 short-wavelength (SWP) spectra were analyzed. These data are summarized in Table 3.

The photometric phases, ϕ, were calculated by assuming the photometric period, $P = 6.95342913$ (Kulkarni & Abhyankar 1980), and the ephemeris of primary minimum, $\mathrm{HJD_{min}} = 2{,}424{,}615.3835$

$$\mathrm{Epoch.phase} = (\mathrm{HJD} - 2{,}424{,}615.3835)/6.95342913 \quad (1)$$

(Etzel 1988). In Tables 2 and 3, HJD is the Heliocentric Julian Date, and Epoch.phase is the whole number epoch with the

TABLE 2

List of Optical Observations

UT Date (1)	HJD −2,400,000 (days) (2)	Epoch.phase (3)	$I(\mathrm{ab}_c)$ (4)	$I(\mathrm{em}_b)$ (5)	$I(\mathrm{em}_r)$ (6)	$V_r(\mathrm{ab}_c)$ (km s^{-1}) (7)	$V_r(2)$ (km s^{-1}) (8)	$O-C$ (km s^{-1}) (9)	Spectroscopic Phase (10)
1985 Feb 25	46,121.8071	3092.923	0.655	0.960	1.235	−10.8	−59.5	3.2	0.394
	46,121.9368	3092.942	0.510	0.920	1.300	...	...	...	...
1985 Feb 26	46,122.7729	3093.062	0.380	1.185	1.025	36.9	42.7	−4.3	0.533
	46,122.8474	3093.073	0.430	1.240	1.105	42.0	54.1	−1.0	0.543
	46,122.9285	3093.085	0.500	1.260	1.170	46.8	62.2	−1.4	0.555
1985 Mar 24	46,148.8856	3096.818	0.800	1.145	1.180	69.9	−120.1	2.8	0.288
1985 Mar 25	46,149.8922	3096.962	0.480	0.960	1.480	43.8	...	...	...
1985 Mar 28	46,152.7334	3097.371	0.750	1.170	1.170	...	...	...	...
1987 Apr 16	46,901.7567	3205.091	0.640	1.340	1.220	61.2	69.4	1.9	0.560
	46,901.8083	3205.098	0.650	1.320	1.240	60.5	77.0	4.3	0.568
	46,901.8374	3205.103	0.660	1.340	1.240	53.8	80.6	5.1	0.572
1987 Apr 17	46,902.7817	3205.238	0.720	1.215	1.190	−2.8	136.6	4.1	0.708
1987 Apr 18	46,903.8010	3205.385	0.665	1.220	1.260	16.3	89.2	−4.2	0.854
1987 Apr 20	46,905.7692	3205.668	0.700	1.350	1.240	33.3	−120.6	−1.0	0.137
1987 May 02	46,917.7436	3207.390	0.610	1.180	1.180	1.8	90.8	0.6	0.859
1987 May 03	46,918.7052	3207.528	0.520	1.240	1.360	−24.3	−26.7	−4.4	0.998
1987 May 04	46,919.7251	3207.675	0.665	1.240	1.140	39.9	−124.2	−1.8	0.144
1987 May 05	46,920.7267	3207.819	0.760	1.150	1.180	52.6	−125.2	−2.4	0.288
1987 May 06	46,921.7241	3207.963	0.400	0.915	1.400	−9.2	−32.6	0.8	0.432
	46,921.7913	3207.972	0.470	1.070	1.740	−6.1	−24.8	0.9	0.442
	46,921.8143	3207.976	0.490	1.160	1.890	−7.5	−22.6	0.4	0.445
1988 May 21	47,302.6684	3262.748	0.670	1.145	1.170	44.0	−135.1	1.2	0.217
	47,302.7044	3262.753	0.660	1.140	1.170	51.0	−133.5	2.7	0.222
1988 May 22	47,303.6591	3262.890	0.680	1.190	1.270	14.8	−84.5	2.1	0.359
	47,303.7218	3262.899	0.675	1.155	1.310	6.2	−76.0	4.7	0.368
	47,303.7523	3262.904	0.660	1.135	1.320	−12.4	−73.0	4.7	0.372
1988 May 23	47,304.6429	3263.032	0.430	1.650	1.110	39.8	24.7	2.7	0.500
	47,304.6701	3263.036	0.390	1.510	1.000	40.9	26.2	1.0	0.504
	47,304.7134	3263.042	0.345	1.370	0.920	43.0	28.7	−1.2	0.511
	47,304.7405	3263.046	0.330	1.300	0.870	45.3	32.6	−0.5	0.515
1988 May 24	47,305.6447	3263.176	0.700	1.200	1.220	14.0	118.2	2.5	0.645
	47,305.7153	3263.186	0.710	1.210	1.210	8.6	120.0	0.4	0.655
1988 May 25	47,306.6893	3263.326	0.690	1.130	1.210	−26.4	122.2	−0.2	0.795
1988 Nov 04	47,470.0043	3286.813	0.730	1.110	1.110	78.4	−121.6	3.6	0.282
1988 Nov 05	47,470.9921	3286.955	0.410	0.850	1.300	−1.9	−41.4	−1.4	0.424
1988 Nov 06	47,471.9933	3287.099	0.560	1.220	1.180	51.6	62.9	−9.6	0.568
1989 Feb 03	47,560.9107	3299.887	0.790	1.220	1.300	26.9	−86.8	2.3	0.355
	47,560.9919	3299.898	0.770	1.170	1.310	49.8	−77.0	4.5	0.367
	47,561.0249	3299.903	0.775	1.170	1.340	52.3	−76.3	2.1	0.371
1989 Feb 04	47,561.7990	3300.014	0.680	2.440	1.720	26.0	13.8	6.1	0.483
	47,561.8334	3300.019	0.660	2.450	1.570	32.0	17.8	6.1	0.488
	47,561.9813	3300.041	0.380	1.420	0.980	35.7	32.3	3.5	0.509
	47,562.0055	3300.044	0.350	1.350	0.940	37.6	34.4	2.8	0.512
1989 Apr 20	47,636.7293	3310.790	0.800	1.220	1.230	46.2	−136.4	−4.8	0.259
	47,636.7744	3310.797	0.780	1.195	1.235	48.7	−131.8	−1.7	0.265
1989 Apr 21	47,637.7765	3310.941	0.550	0.930	1.330	−8.0	−39.6	11.4	0.409
1989 Apr 23	47,639.7354	3311.223	0.770	1.250	1.230	−3.4	136.6	6.7	0.691
	47,640.7299	3311.366	0.665	1.200	1.320	12.5	99.1	−6.0	0.834
1990 Feb 17	47,939.8551	3354.384	0.645	1.210	1.280	−2.8	91.5	−3.2	0.852
1990 Feb 18	47,940.8822	3354.532	0.380	1.160	1.370	−27.7	−31.8	−7.7	0.000
1991 Feb 26	48,313.8742	3408.173	0.600	1.180	1.180	1.2	119.1	5.1	0.641
1991 Feb 27	48,314.8265	3408.310	0.760	1.160	1.210	−33.3	125.1	−2.4	0.778
1991 Mar 04	48,319.8424	3409.031	0.510	1.720	1.120	23.0	13.4	−7.3	0.499
	48,319.8759	3409.036	0.460	1.580	1.040	24.3	17.4	−7.2	0.504
	48,319.9089	3409.041	0.420	1.450	0.960	24.8	19.2	−9.2	0.509
	48,319.9510	3409.047	0.400	1.370	0.900	29.6	23.8	−9.4	0.515
1991 Mar 05	48,320.8750	3409.180	0.630	1.240	1.200	−11.2	113.2	−3.6	0.648
1994 Apr 01	49,443.7821	3570.670	0.720	1.460	1.370	27.9	−123.4	−4.5	0.136
1994 Apr 02	49,444.7740	3570.812	1.065	1.275	1.260	74.8	−127.9	−1.7	0.279
1994 Apr 03	49,445.7918	3570.959	0.550	0.970	1.480	−8.5	−36.7	2.2	0.425
1994 Apr 05	49,447.8002	3571.248	0.750	1.350	1.230	2.0	133.7	0.6	0.714
1994 Jun 02	49,505.6359	3579.565	0.57	1.07	1.24	−4.9	−44.3	−2.6	0.031
1994 Jun 03	49,506.6465	3579.711	0.71	1.06	1.15	48.4	−121.8	1.0	0.177

TABLE 2—*Continued*

UT Date (1)	HJD −2,400,000 (days) (2)	Epoch.phase (3)	$I(\mathrm{ab}_c)$ (4)	$I(\mathrm{em}_b)$ (5)	$I(\mathrm{em}_r)$ (6)	$V_r(\mathrm{ab}_c)$ (km s^{-1}) (7)	$V_r(2)$ (km s^{-1}) (8)	$O-C$ (km s^{-1}) (9)	Spectroscopic Phase (10)
1994 Jun 04	49,507.6476	3579.854	0.79	1.10	1.17	9.8	−104.2	−4.6	0.321
1994 Jun 05	49,508.6534	3579.999	0.82	1.73	1.83	−2.6	3.3	0.7	0.465
	49,508.6795	3580.003	0.82	1.84	1.76	0.3	6.1	0.4	0.469
1994 Jun 06	49,509.6547	3580.143	0.81	1.21	1.14	6.5	111.3	3.5	0.609
1994 Jun 07	49,510.6480	3580.286	0.76	1.12	1.09	−24.2	143.6	1.9	0.752
1994 Jun 08	49,511.6477	3580.430	0.54	1.20	1.11	20.1	73.7	−0.1	0.896
1994 Dec 02	49,688.9327	3605.926	0.57	0.99	1.25	−13.3	−55.0	−0.0	0.392
	49,688.9703	3605.931	0.54	0.95	1.26	−8.3	−51.5	−0.4	0.397
	49,689.0150	3605.938	0.50	0.92	1.25	−3.0	−46.1	0.1	0.403
	49,689.0331	3605.940	0.48	0.91	1.26	−1.9	−45.1	−0.7	0.406
	49,689.0584	3605.944	0.45	0.89	1.24	3.00	−42.4	−0.8	0.410
1994 Dec 03	49,689.9092	3606.066	0.34	1.26	0.95	36.3	54.6	−1.4	0.532
	49,689.9404	3606.071	0.36	1.24	0.98	38.6	59.1	−0.3	0.537
	49,689.9815	3606.077	0.38	1.22	1.01	43.6	62.7	−1.1	0.542
	49,690.0391	3606.085	0.41	1.21	1.07	44.7	69.1	−0.8	0.551
1994 Dec 04	49,690.9599	3606.217	0.68	1.14	1.13	−24.2	139.4	1.8	0.683
	49,691.0158	3606.225	0.67	1.13	1.13	−30.1	140.4	1.1	0.691
	49,691.0562	3606.231	0.67	1.13	1.10	−27.6	143.1	2.8	0.697
1994 Dec 08	49,694.9391	3606.790	0.78	1.17	1.17	50.8	−122.7	0.4	0.255
	49,694.9881	3606.797	0.79	1.17	1.17	55.2	−120.2	1.2	0.262
	49,695.0535	3606.806	0.80	1.18	1.18	63.7	−120.0	−0.9	0.272
1996 Feb 16	50,129.7633	3669.323	0.75	1.12	1.13	−27.8	132.3	−1.3	0.789
	50,129.8095	3669.330	0.73	1.12	1.14	−29.6	129.4	−2.0	0.795
	50,129.8569	3669.337	0.73	1.12	1.17	−32.5	127.6	−1.4	0.802
1996 Feb 17	50,130.7779	3669.469	0.47	1.26	1.13	0.5	42.6	0.3	0.935
	50,130.8203	3669.475	0.45	1.25	1.14	1.2	39.9	2.8	0.941
	50,130.8617	3669.481	0.42	1.26	1.16	−0.6	34.4	2.5	0.947
	50,130.9299	3669.491	0.39	1.28	1.19	−1.5	26.3	3.0	0.956
	50,130.9601	3669.496	0.38	1.26	1.21	−2.0	24.3	4.8	0.961
	50,130.9929	3669.500	0.38	1.25	1.22	−2.4	17.1	1.7	0.966
1996 Feb 18	50,131.7747	3669.613	0.67	1.32	1.23	32.4	−80.7	−3.5	0.078
	50,131.8171	3669.619	0.67	1.31	1.22	36.5	−83.4	−2.2	0.084
	50,131.8638	3669.625	0.68	1.30	1.23	35.6	−86.1	−0.5	0.091
	50,131.9239	3669.634	0.68	1.31	1.22	34.2	−90.5	0.3	0.099
	50,131.9604	3669.639	0.68	1.31	1.22	38.0	−94.2	−0.1	0.105
1996 Feb 19	50,132.7798	3669.757	0.75	1.11	1.17	64.9	−125.4	1.7	0.222
	50,132.8731	3669.771	0.73	1.13	1.15	...	...	...	...
	50,132.9687	3669.784	0.74	1.09	1.17	...	...	...	...
1997 May 31	50,599.6386	3736.898	0.72	1.17	1.26	30.5	−77.0	−2.0	0.363
1997 Jun 01	50,600.6198	3737.039	0.43	1.57	1.02	31.5	33.4	−0.4	0.504
1997 Jun 02	50,601.6166	3737.187	0.59	1.17	1.16	−15.9	128.5	2.5	0.647
1997 Jun 03	50,602.6167	3737.326	0.69	1.13	1.17	−23.2	133.0	0.0	0.791
1997 Jun 04	50,603.6209	3737.471	0.42	1.22	1.17	5.2	39.9	−1.5	0.935
1997 Jun 05	50,604.6189	3737.614	0.62	1.32	1.18	−7.3	−79.8	−1.9	0.079
1997 Jun 07	50,606.6175	3737.902	0.57	1.07	1.16	−15.4	...	...	...
1999 Jan 13	51,191.9724	3822.084	0.440	1.270	1.100	47.7	57.3	−1.2	0.548
1999 Jan 14	51,192.9756	3822.228	0.640	1.190	1.180	−8.1	130.1	−0.0	0.692
1999 Jan 15	51,194.0161	3822.378	0.690	1.160	1.230	3.3	102.2	1.3	0.842
1999 Jan 17	51,196.0222	3822.666	0.610	1.240	1.110	38.3	−116.1	0.3	0.130
1999 Jan 18	51,196.9780	3822.804	0.740	1.100	1.140	56.9	−126.4	3.0	0.268
1999 Jan 19	51,197.9733	3822.947	0.470	0.870	1.240	−15.6	−50.5	−0.6	0.411
	51,198.0140	3822.953	0.420	0.840	1.240	−12.4	−45.6	−0.1	0.417
	51,198.0353	3822.956	0.400	0.825	1.230	−11.8	−43.3	−0.2	0.420
1999 Nov 21	51,504.0479	3866.965	0.400	0.880	1.400	−8.1	−34.6	1.7	0.428
2001 Jan 05	51,915.0339	3926.070	0.380	1.390	1.000	46.2	49.0	1.3	0.533
2001 Jan 07	51,916.9961	3926.352	0.810	1.220	1.270	23.8	110.6	−3.5	0.815

NOTE.—$I(\mathrm{ab}_c)$ is the normalized flux (depth) of the central absorption of Hα; $I(\mathrm{em}_b)$ is the strength of the blue emission peak; $I(\mathrm{em}_r)$ is the strength of the red emission peak; $V_r(\mathrm{ab}_c)$ is the radial velocity of the central absorption; $V_r(2)$ is the radial velocity of the secondary; and $O-C$ is the $O-C$ for the radial velocities of the secondary.

TABLE 3
HIGH-RESOLUTION *IUE* OBSERVATIONS

UT Date	HJD −2,400,000	Epoch.phase	Region, No.	Observers	V_r (km s^{-1})
1980 Dec 28	2,444,602.3014	2874.397	LWP 10176HL	Plavec	52.2
1980 Dec 29	2,444,602.5507	2874.433	LWP 17802HL	Peters	65.4
1987 Feb 23	2,446,850.1432	3197.668	LWP 24387HL	Eaton	69.3
1990 Apr 23	2,448,005.3561	3363.804	LWP 24393HL	Eaton	...
1992 Dec 02	2,448,958.6272	3500.898	LWR 09595HL	Kondo	−20.7
	2,448,959.4625	3501.018	LWR 09597HL	Kondo	−23.2
1980 Nov 10	2,444,554.3882	2867.507	SWP 10585HL	Kondo	7.7
1980 Dec 28	2,444,602.3738	2874.408	SWP 10912HL	Kondo	−18.9
1981 Jan 11	2,444,616.2290	2876.400	SWP 11024HL	Peters	−25.4
1981 Feb 25	2,444,661.3663	2882.892	SWP 13361HL	Peters	63.6
1987 Feb 23	2,446,850.0810	3197.659	SWP 30367HL	Plavec	61.9
1990 Apr 19	2,448,001.4831	3363.247	SWP 38633HL	Peters	18.1
1990 Apr 21	2,448,003.3308	3363.513	SWP 38643HL	Peters	11.4
1990 Apr 22	2,448,004.2864	3363.650	SWP 38651HL	Peters	47.7
1990 Apr 23	2,448,005.2903	3363.795	SWP 38665HL	Peters	73.2
1992 Dec 02	2,448,958.5819	3500.891	SWP 46386HL	Eaton	70.2
	2,448,959.3446	3501.001	SWP 46392HL	Eaton	...

photometric phase, ϕ, listed after the decimal point (see eq. [1]). The phase coverage of the spectra is illustrated in Figure 1.

3. THE OPTICAL SPECTRA

This section describes the analysis of the optical spectra. In § 3.1 we derive precise orbital elements and improve the values for the absolute dimensions of the system based on a new velocity curve for the secondary. In § 3.2 we discuss the central absorption of the Hα line that is most closely associated with the primary star. In § 3.3 we describe the calculation of synthetic Hα spectra with the new code called SHELLSPEC (Budaj & Richards 2004; BRM05). Model spectra were calculated for the stars, accretion disk, and gas stream. These synthetic spectra were compared with the observed spectra and both were later used to make reconstructed images of the accretion structures in the binary (see § 5).

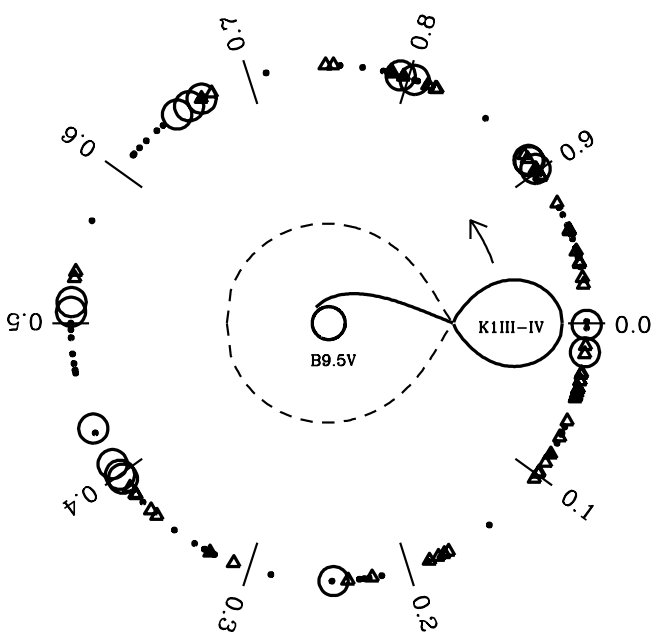

FIG. 1.—Phase coverage of TT Hya showing the KPNO data collected from 1985 February to 1991 March (*open triangles*) and from 1994 April to 2001 (*filled circles*), as well as the high-resolution *IUE* data collected from 1980 December to 1992 December (*large open circles*). [*See the electronic edition of the Journal for a color version of this figure.*]

3.1. *Radial Velocity Measurements of the Secondary*

The spectral lines of the secondary are seen more clearly in our optical spectra because they are much sharper than the lines of the primary. They are more accurate tracers of the orbital motion than the lines of the primary, which are highly broadened by the stellar rotation and distorted by the presence of the accretion disk. Hence, orbital elements based on the lines of the primary are not as precise as those derived from the lines of the secondary.

The radial velocities were determined using the cross-correlation technique, and a template based on synthetic spectra was created for this procedure. First, the model atmosphere of the secondary star was obtained by interpolating in the Kurucz (1993a) $T_{\rm eff}$ − log g grid and assuming solar abundances and a microturbulence of 2 km s^{-1}. Next, the intrinsic synthetic stellar spectrum of the secondary emerging from this atmospheric model (flux per unit surface area) was calculated using the code called SYNSPEC (Hubeny et al. 1994), as modified by Krtička (1998). Here again, solar abundances and a microturbulence of 2 km s^{-1} were assumed. The synthetic spectrum was then convolved with the rotational ($v \sin i = 43$ km s^{-1}; Eaton & Henry 1992) and instrumental profiles. Subsequently, this synthetic spectrum was diluted with the featureless continuum of the primary assuming a known L1/L2 ratio, where L1 and L2 are the luminosities corresponding to the Hα continuum of the primary and secondary, respectively. This diluted spectrum was then used as a template for the radial velocity measurements. The radial velocities of the secondary star were measured using the cross-correlation of the observed spectra with this template synthetic spectrum, omitting the region near Hα. Six spectra at phases 3092.942, 3096.962, 3097.371, 3669.771, 3669.784, and 3737.902 were excluded from the measurements due to either a low signal-to-noise ratio or heavy blending by terrestrial lines; hence, a total of 113 highly reliable radial velocity measurements of the secondary star were obtained. These are listed under $V_r(2)$ in column (8) of Table 2. Our measurements have more than quadrupled the previous number of radial velocity measurements of the secondary since Popper's work. Moreover,

TABLE 4
ORBITAL ELEMENTS OF TT HYA

Property (1)	1994–2001 Data (Period Fixed[a]) (2)	1985–2001 Data (Period Fixed[a]) (3)	1956–2001 Data[b] (Period Fixed[a]) (4)	1956–2001 Data[b] (Period Not Fixed) (5)
Systemic velocity, V_0 (km s^{-1})	8.43 ± 0.27	8.56 ± 0.28	8.43 ± 0.27	8.34 ± 0.26
Velocity semiamplitude, K_2 (km s^{-1})	135.76 ± 0.40	135.55 ± 0.41	135.12 ± 0.40	135.13 ± 0.37
Eccentricity, e	0.0214 ± 0.0028	0.0217 ± 0.0029	0.0204 ± 0.0029	0.0211 ± 0.0027
Longitude of periastron, ω (deg)	99.9 ± 7.5	100.7 ± 7.4	103.4 ± 7.9	101.6 ± 7.2
Epoch of periastron, T_0 (days)	2,450,006.09 ± 0.14	2,450,006.07 ± 0.15	2,450,006.14 ± 0.15	2,450,006.10 ± 0.14
Orbital period, P (days)	6.95342913	6.95342913	6.95342913	6.953484 ± 0.000012
Mass function, $f(m)$	1.806 ± 0.016	1.797 ± 0.016	1.781 ± 0.016	1.781 ± 0.015
Semimajor axis, $a_2 \sin i$ (10^7 km)	1.2978 ± 0.0038	1.2957 ± 0.0039	1.2917 ± 0.0038	1.2917 ± 0.0036
Standard deviation of fit, σ (km s^{-1})	2.0	2.9	3.2	3.0
Optimum fit	Best photometry	...	...	Best spectroscopy

[a] Photometric period from Kulkarni & Abhyankar (1980).
[b] Includes data from Popper (1989) (see Fig. 2).

the much improved precision and phase coverage allowed us to examine whether Algol-type binaries might have noncircular orbits.

The derivation of orbital elements for TT Hya was performed using the SBCM code of Morbey & Brosterhus (1974). Table 4 lists the resulting orbital elements: systemic velocity, V_0; velocity semiamplitude, K_2; orbital eccentricity, e; longitude of periastron, ω; epoch of the periastron, T_0; orbital period, P; mass function, $f(m)$; semimajor axis, $a_2 \sin i$; and standard deviation of the fit, σ. First, the original 27 radial velocity measurements of Popper (1989) from 1956 to 1977 were reanalyzed and a mean standard deviation, $\sigma \sim 5.1$ km s^{-1}, was obtained. Next, we analyzed our KPNO data in three groups by date, 1985–1991, 1994–2001, and 1985–2001, and found solutions with $\sigma = 4.4$, 2.0, and 2.9 km s^{-1}, respectively. Finally, we combined our data with those of Popper (1989) to obtain a data set of 140 measurements over an extended baseline of 45 years. The measurements were weighted according to the inverse square of their standard deviation, which resulted in weights of 0.15 for the 1956–1977 data from Popper (1989), 0.21 for the 1985–1991 data, and 1.0 for the 1994–2001 data. Since the precision of the photometric period of the Kulkarni & Abhyankar (1980) was uncertain, we calculated four velocity curve solutions. The orbital period was fixed at the value published by Kulkarni & Abhyankar (1980) for the analysis of (1) the 1994–2001 data, (2) the 1985–2001 data, and (3) the complete data set from 1956 to 2001, which included Popper's measurements (see Table 4, cols. [2]–[4]). In the final case, the 1956–2001 data were analyzed with the period as a free parameter within SBCM (Table 4, col. [5]). The elements derived from column (5) of Table 4 were used to calculate the $O - C$ and spectroscopic phases listed in Table 2.

The differences in the orbital elements listed in Table 4 are very small. The orbital solution derived from our most accurate data (1994–2001 data; col. [2]) is to be preferred. However, the results listed in column (5) provide the best orbit based entirely on spectroscopic data. We note that the orbital period of 6.953429 days derived by Kulkarni & Abhyankar (1980) is well outside the error bars of the new spectroscopic solution of $P = 6.953484 \pm 0.000012$ days. This spectroscopic orbital solution and radial velocity measurements are illustrated in Figure 2, and the $O - C$ residuals are shown in Figure 3. Figure 3 shows that Popper's measurements (Popper 1989) tend to smooth the amplitude of the radial velocity curve at the quadratures.

Assuming $a_2 \sin i = 1.2978 \times 10^7$ km from the solution in Table 4 (col. [2]) based on the high-accuracy 1994–2001 data and an inclination and mass ratio from Van Hamme & Wilson (1993), we obtain $a = 23.04\ R_\odot$ and $M_1 + M_2 = 3.40\ M_\odot$. The stellar masses were computed directly from the derived semimajor axis using Kepler's third law, assuming a known mass ratio. However, since Van Hamme & Wilson (1993) found that $a = 22.63\ R_\odot$, we calculated improved stellar radii by rescaling the Van Hamme & Wilson (1993) radii by a factor of 23.04/22.63 or 1.018. This simple scaling of the system dimensions is necessitated by the absence of adequate new photometry, especially at red or near-infrared wavelengths. Moreover, we hope that new simultaneous light-curve and velocity curve solutions will be completed to further improve the parameters of this system. The new radii and other derived system parameters are listed in Table 5. Here the column labeled "VW" lists the results from Table 4b of Van Hamme & Wilson (1993), while the last column gives our improved values. If we assume that $R/d = 9.78$ (Plavec 1988), where R is the radius of the primary in $R_\odot$ and d is the distance to the system in kpc, then we obtain a new distance $d = 203$ pc to TT Hya. This new value is still not in good agreement with the *Hipparcos* distance of 154 pc (Perryman et al. 1997). This means that either the *Hipparcos* parallax was overestimated or the

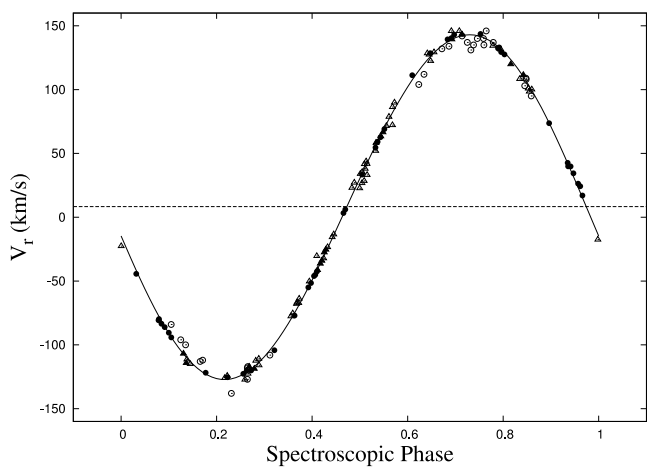

FIG. 2.— Velocity curve of TT Hya based on elements from col. (5) of Table 4, showing the TT Hya spectra obtained from 1985 February to 1991 March (Peters; *open triangles*), 1994 April (Peters; *filled triangles*), 1994 June–1997 June (Richards, Albright, & Koubský; *filled circles*), 1999 January–2001 January (Peters; *filled triangles*), and the 1956–1977 data from Popper (1989) (*open circles*). The latest KPNO data from 1994 to 2001 (*filled circles and filled triangles*) constitute the best data set. The phases given here are spectroscopic phases measured from periastron.

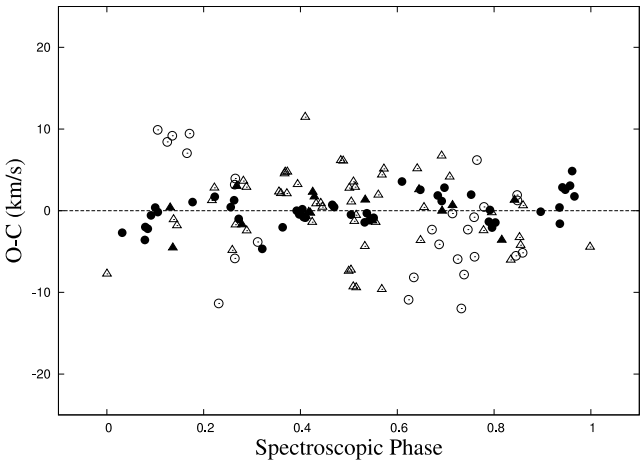

FIG. 3.—Residuals of the radial velocity curve of TT Hya (elements Table 4, col. [5]), showing the KPNO spectra obtained from 1985 to 2001 and the data from Popper (1989) (*open circles*). The symbols have the same notation as in Fig. 2. The phases given here are spectroscopic phases measured from periastron. Note that the filled symbols representing the 1994–2001 data have consistently lower $O - C$ values than the other data.

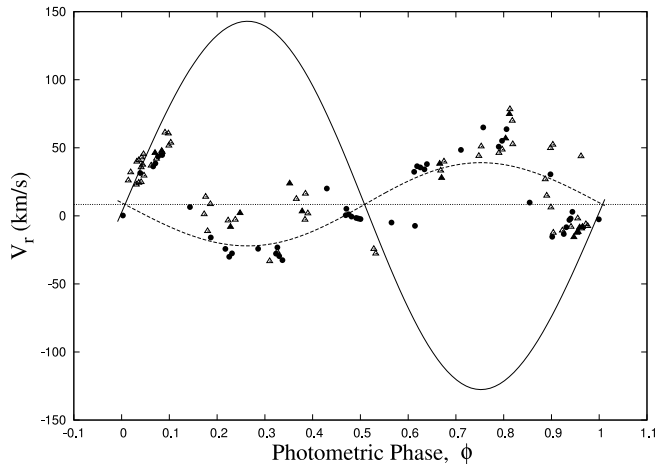

FIG. 4.—Radial velocity, $V_r(\mathrm{ab}_c)$, of the central absorption of the Hα line. The solid line is the velocity curve of the secondary, and the dashed line is the velocity curve of the primary derived using the Van Hamme & Wilson (1993) solution (see § 3.2). The symbols have the same notation as in Fig. 2. The phases shown are photometric phases.

temperature of 9900 K assumed by Plavec (1988) was overestimated, i.e., his value of R/d was underestimated.

Table 4 also shows that the eccentricity differs from zero by more than 7 σ and the standard deviation of the best photometric fit is 2.0 km s^{-1}, a significant improvement over the previous eccentricity and circular orbit derived by Popper (1989). An eccentric orbit for the secondary star could imply that the mass transfer process may not be uniform. Based on our analysis of the spectra, this process could be intensified at periastron, when the Roche lobe shrinks, and attenuated at apastron. Assuming that more material is released at periastron (photometric phase, $\phi = 0.537$) than at apastron, and that it takes time for this material to interact with the disk, get heated, and become luminous, then enhanced Hα emission should be detected with the stronger blue peak at the phases shortly after $\phi = 0.55$. Evidence of such enhanced emission was found at phases $\phi = 0.60$–0.65 (see BRM05, their Fig. 6); consequently, enhanced emission near periastron is a viable possibility. Similar observations in other Algol-type binaries with nonzero eccentricities would provide stronger evidence of the association with periastron. Moreover, these results may explain the RZ Cas system in which intensified pulsations of the primary star are strongest shortly after primary eclipse (Lehmann & Mkrtichian 2004), which occurs near periastron.

3.2. *Radial Velocity of the* Hα *Central Absorption*

The Hα line has a complicated shape because it contains double-peaked emission with a central absorption. Table 2 lists our measurements of the normalized fluxes of the blue and red emission peaks [$I(\mathrm{em}_b)$, $I(\mathrm{em}_r)$] and the central absorption [$I(\mathrm{ab}_c)$], as well as the radial velocity measurements of the central absorption [$V_r(\mathrm{ab}_c)$]. The central absorption (or depression) in the Hα line profile is the strongest feature in our spectra that can be ascribed (at least partly) to the primary star.

TABLE 5
THE PHYSICAL PROPERTIES OF TT HYA

Property	VW[a]	This Paper
Mass ratio, q	0.2261	0.2261
Inclination, i (deg)	82.84	82.84
Semimajor axis, a ($R_\odot$)	22.63	23.04
Mass, M_1 ($M_\odot$)	2.63	2.77
Mass, M_2 ($M_\odot$)	0.59	0.63
Radius, R_1 ($R_\odot$)	1.95	1.99
Radius, R_2 ($R_\odot$)	5.87	5.98

[a] These values are from Table 4b of Van Hamme & Wilson (1993).

The radial velocity of the Hα line core, $V_r(\mathrm{ab}_c)$, is shown in Figure 4. These measurements reflect the motion of the primary star but are distorted by several effects at different phases. Near first quadrature (phase, $\phi \sim 0.1$–0.4), the spectrum shows blueshifted absorption. Closer to secondary eclipse ($\phi \sim 0.5$), we do not observe any significant negative velocities and thus cannot confirm previous suggestions of mass outflow at these phases (Peters 1989). The opposite quadrature from $\phi \sim 0.6$–0.9 has somewhat higher redshifted velocities since the gas stream and disk that project onto the primary star surface have a considerable radial, infalling component of the velocity.

Near primary eclipse the velocities of the central Hα absorption differ greatly from those predicted by the orbital motion of the primary. It might be expected that the gradual occultation of the rapidly rotating primary would considerably affect the measured radial velocities; however, this rotational effect can only operate within the partial eclipse from $\phi = 0.95$ to 0.05 and the velocity curve is distorted over a much broader interval from $\phi = 0.9$ to 0.1. Moreover, the rotational effect would predict positive velocities from $\phi = 0.95$ to 1.0 and negative velocities from $\phi = 0.0$ to 0.05, while the opposite trend is observed. Another explanation of this effect is thus necessary. The eclipse of the approaching edge of the disk from $\phi = 0.9$ to 1.0 removes the blueshifted emission peak, which should manifest as blueshifted absorption in the observed Hα profile (with an opposite effect for $\phi = 0.0$–0.1). This phenomenon influences the broad shape of the Hα core but is not the predominant cause of the anomalous radial velocity measurements near primary eclipse. It is the secondary star that is mainly responsible for the effect. Although its intrinsic Hα line is rather weak, it is narrow and can considerably affect the radial velocity measurements of the center of Hα absorption, particularly at the phases when both components of Hα (from the primary and secondary) are aligned and become unresolved. At these phases, the secondary component of Hα determines the deepest point of the whole Hα feature that was

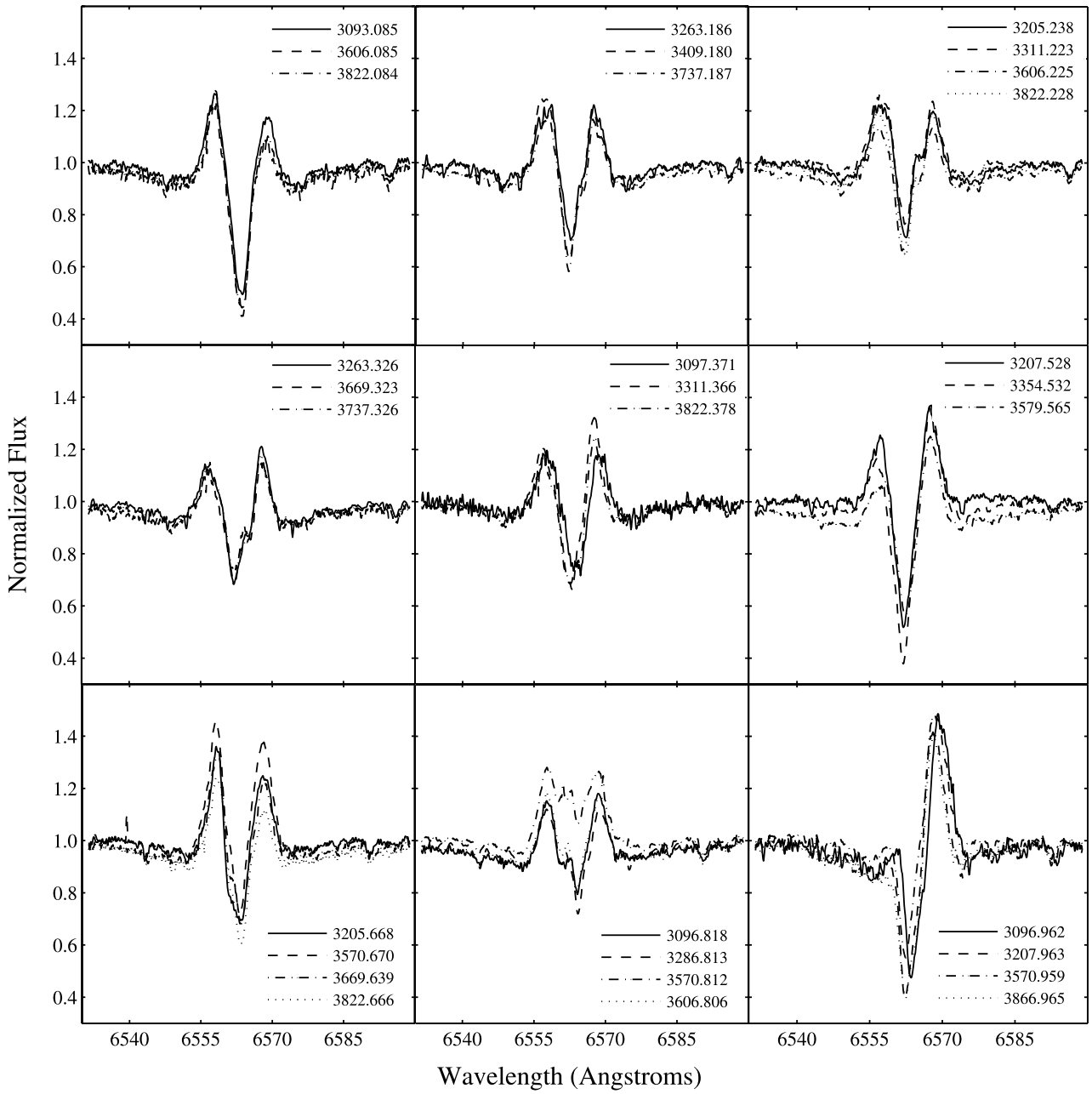

FIG. 5.—Comparison of the observed Hα spectra at different epochs for phases near $\phi = 0.08$, 0.19, 0.23, 0.33, 0.37, 0.54, 0.67, 0.81, and 0.96. There is remarkable similarity between the spectra at the epochs separated by 833 cycles, except that the spectra at epoch 3570 had significantly stronger disk emission than the other spectra. [*See the electronic edition of the Journal for a color version of this figure.*]

used in radial velocity measurements. The measurements of Hα absorption near primary eclipse are in excellent agreement with the velocity curve of the secondary, and similar measurements performed on the synthetic spectra of the stars plus disk also reveal a transition near primary eclipse where the Hα absorption ceases to follow the velocity curve of the primary and instead matches that of the secondary. A qualitatively similar effect is observed near secondary eclipse, although in this case the amplitude of the measured radial velocities is slightly less than predicted by the secondary velocity curve, presumably a result of the partial obscuration of the secondary.

Future radial velocity measurements of the primary from weaker lines in the infrared, as well as *R*-band and infrared photometry (see, e.g., Richards 1990), might improve the parameters of the system considerably, specifically the mass ratio and the temperature of the secondary star.

3.3. *The "REBECA" Diagram*

The variability of the Hα line profile with epoch is illustrated in Figure 5 for phases near $\phi = 0.08$, 0.19, 0.23, 0.33, 0.37, 0.54, 0.67, 0.81, and 0.96. This figure shows that the spectra obtained in 1994 April (epoch 3570) had significantly stronger disk emission than the other spectra. The emission strength returned to normal by 1994 June (epoch 3579).

The three major characteristics of the complicated Hα profile, Red Emission, Blue Emission, and Central Absorption [$I(\mathrm{em}_r)$, $I(\mathrm{em}_b)$, $I(\mathrm{ab}_c)$], can be plotted as a function of phase, ϕ, in what we call a "REBECA" diagram. BRM05 illustrated how various

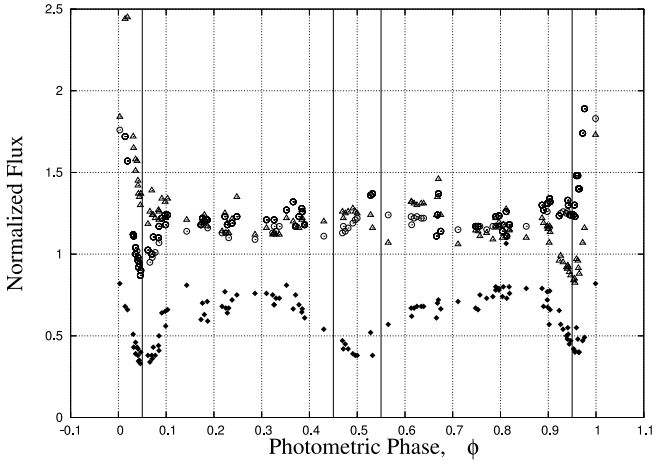

FIG. 6.—REBECA diagram for the 1985–2001 data showing the behavior of the emission strength and central absorption depth around the orbit of TT Hya. *Triangles*: highest normalized flux of the blue emission peak; *circles*: flux of the red emission; *diamonds*: depth of the central depression. The vertical lines indicate the start and the end of primary and secondary eclipse. [*See the electronic edition of the Journal for a color version of this figure.*]

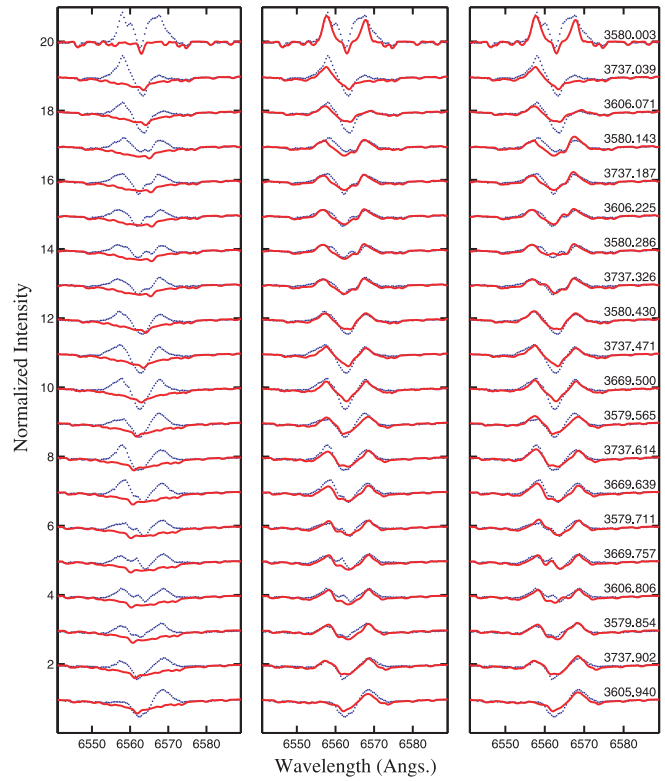

FIG. 7.—Comparison of the observed (*dotted line*) and synthetic (*solid line*) Hα spectra of TT Hya. The epochs and orbital phases are listed to the right of the figure. The synthetic spectra include calculations of stars only (*left*), stars and disk (*middle*), and stars, disk, and gas stream (*right*). There is a significant improvement in the fit between the observed and synthetic spectra once the accretion disk is included, but only a minor improvement once the gas stream is included in the model.

structures could be identified in this diagram (see Fig. 6 of BRM05). We have revised their figure to include all TT Hya spectra from 1985 to 2001 (see Fig. 6). Phases $\phi = 0.1$–0.3 show comparable intensity in the blue-red emission peaks, while the red emission is slightly stronger at $\phi = 0.3$–0.4. BRM05 speculated that such an effect, if accompanied by the reverse (blue emission stronger) during the mirror phases ($\phi = 0.6$–0.7), could indicate the presence of circumstellar matter in the vicinity of the secondary star between the C1 and C2 surfaces. The new 1985–2001 observations at $\phi = 0.3$–0.4 confirm that the red emission is stronger, while at $\phi = 0.6$–0.7 the blue emission is stronger. However, the above-mentioned idea of BRM05 probably cannot explain the effect since it would require a circumstellar matter between C1 and C2 surfaces projecting onto the surface of the secondary with a considerable outflowing velocity component (relative to the secondary star) at $\phi = 0.3$–0.4 and inflowing velocity component during $\phi = 0.6$–0.7, which seems unlikely. At $\phi = 0.4$–0.5, the blue emission is stronger than the red emission and both emissions increase slightly. According to BRM05, this is caused by the extra absorption of the secondary's light in the receding part of the disk and by the eclipse of the secondary star. The calculations of BRM05 predicted that the reverse should be seen during the mirror phases ($\phi = 0.5$–0.6). Our new observations from 1985 to 2001 strongly confirm the presence of this effect. The central absorption gets progressively deeper when approaching the secondary eclipse as described in BRM05.

The blue and red emission seen during $\phi = 0.7$–0.88 seem fairly symmetric. Starting at about $\phi = 0.88$, all three parameters [$I(\mathrm{em}_b)$, $I(\mathrm{em}_r)$, $I(\mathrm{ab}_c)$] change dramatically. The blue emission decreases rapidly due to the eclipse of the disk, while the red emission gets slightly stronger. At about $\phi = 0.95$, both emissions soar as we go into total eclipse, and the reverse effects are observed during $\phi = 0.0$–0.1. This behavior was explained by BRM05; however, the blue emission at about phase 0.02 seems surprisingly strong. The "W" shape of the central absorption pattern near primary eclipse, from $\phi = 0.88$ to 0.1, was qualitatively explained by the calculations of BRM05. In addition, they suggested the presence of cooler circumstellar matter around the secondary star, which would produce an excess absorption in the core of Hα at these phases. Using O I λ7774 spectroscopy, Etzel et al. (1995) identified similar interesting effects of disks and streams in several Algols around or near both eclipses. We anticipate that synthetic spectra generated from the output of hydrodynamic simulations may more clearly explain the "W" behavior of the central absorption at these eclipse phases.

3.4. *Observed and Synthetic* Hα *Spectra*

The behavior of the line shape was studied in detail by BRM05. In that paper we showed that the emission peaks originated from the disk and that both the emission and central absorption varied with phase. In addition, we proposed a quantitative empirical model of the disk that could account for the behavior of the observed Hα line profiles. However, BRM05 found that there remained a difference between the observed and synthetic spectra that could be improved if the primary star was assigned a lower effective gravity than derived earlier and the gas stream was considered in the calculations. In this paper we have recalculated the synthetic spectra by including the gas stream as well as the stars and accretion disk in the model. These changes improved the fits between the observed and synthetic spectra at all phases outside of primary eclipse, $\phi = 0.225$–0.854 (see Fig. 7), while having almost no effect on the primary eclipse spectra.

The SYNSPEC code (Hubeny et al. 1994) was used to calculate the new intrinsic (not rotationally broadened) spectrum of the primary assuming a lower surface gravity of $\log g = 3.5$, microturbulence of $v_{\mathrm{trb}} = 2$ km s^{-1}, and solar abundances, as well as Kurucz models and line lists (Kurucz 1993a, 1993b). The synthetic spectrum of the secondary was based on the parameters

TABLE 6
Adopted and Derived Properties of TT Hya from *IUE* SWP Spectra

Parameter	Value	Source
Primary		
Mass, M ($M_\odot$)	2.77	MBRKP
Radius, R ($R_\odot$)	1.99	MBRKP
Surface gravity, $\log g$	4.	MBRKP
Temperature, T (K)	10,000	MBRKP
Rotational velocity, $v \sin i$ (km s^{-1})	168	E
Limb-darkening coefficient, u	0.5	VW
Disk		
Inclination, i (deg)	82.84	VW
Vertical half-thickness, α ($R_\odot$)	2	BRM
Inner radius, $R_{\rm in}$ ($R_\odot$)	2	BRM
Outer radius, $R_{\rm out}$ ($R_\odot$)	10	BRM
Density, $\rho(R_{\rm in})$ (g cm^{-3})	5×10^{-14}	MBRKP, BRM
Temperature, T (K)	7000	MBRKP
Density exponent,[a] η	-1	BRM
Microturbulence, $v_{\rm trb}$ (km s^{-1})	30	BRM

[a] η is the exponent of the power law in the radial density profile (see BRM).
Sources.—(BRM) Budaj et al. 2005; (E) Etzel 1988; (MBRKP) This work; (VW) Van Hamme & Wilson 1993.

used in BRM05. New composite synthetic spectra of the stars, disk, and gas stream were calculated using the SHELLSPEC code (Budaj & Richards 2004), for phases corresponding to the observations. The gas stream was treated as a simple cylinder located along the predicted free-fall path with approximately free-fall velocities. Since the disk extends almost to the Roche lobe and has a thickness of 2 $R_\odot$ above (and below) the orbital plane, the radius of the stream cylinder was set to $R = 3\ R_\odot$ to produce an overlap between the gas stream and disk locations. This overlap permitted the stream to flow through only above and below the disk. The density, temperature, and velocity field of the disk were assigned a higher priority than the gas stream in the overlap region.

Initially, a gas stream temperature of $T = 8000$ K was chosen to correspond to the peak in Hα emissivity. The estimated density of the stream at the starting point (2×10^{-14} g cm^{-3}) was chosen to improve the fit between the observed and synthetic emission at the quadratures of the orbit and during the eclipses. For these calculations, the density was allowed to vary along the stream to satisfy the continuity equation. The density of the disk at the inner radius was 3.3×10^{-14} g cm^{-3}, and the temperature of the disk was $T = 7000$ K. Note that this density derived from the Hα line is very close to the value of 5×10^{-14} g cm^{-3} obtained from the *IUE* spectra (see § 4 and Table 6), but the *IUE* solution produced a better fit to the data. The electron number densities in the disk and stream were calculated from the temperature, density, and chemical composition using the Newton-Raphson linearization method. All of the other parameters of the system were the same as in Table 1 of BRM05. The comparison between the observed and synthetic spectra in Figure 7 demonstrates that the inclusion of the gas stream in the synthetic spectra slightly improves the fit between observation and theory, particularly near the quadratures.

The mass transfer rate can be estimated from the velocity, density, and cross section (the two semicircular sectors) of the gas stream above and below the disk. We obtained a rate of $\sim2\times10^{-10}\ M_\odot$ yr^{-1}, 2 orders of magnitude higher than the lower limit of $10^{-12}\ M_\odot$ yr^{-1} obtained by Peters & Polidan (1998). Since the temperature of the stream was chosen to correspond to the peak Hα emissivity, our value of the mass transfer rate is still a lower limit. This rate depends essentially on the equivalent width of the excess emission corresponding to the stream, i.e., on the stream temperature and density, but not significantly on any particular choice of stream geometry.

4. THE ULTRAVIOLET SPECTRA

The ultraviolet spectra of TT Hya analyzed in this work were derived from *IUE* spectra collected from 1980 to 1992 (see § 2). A few of these spectra were studied by Plavec (1988), but his analysis focused on the low-resolution spectra and included only two out-of-eclipse high-resolution *IUE* spectra. Since that time, 17 high-resolution spectra were obtained with the *IUE* telescope, including two during total eclipse. These data are summarized in Table 3. Only the high-resolution spectra have been analyzed in this work since the low-resolution spectra are not suitable for our radial velocity studies.

4.1. *Radial Velocities of the Primary from UV Lines*

In the optical spectra, there are very few absorption lines of the primary, and these are often heavily distorted and contaminated by emission features. However, the ultraviolet lines can be used to measure radial velocities, which are crucial for establishing a precise mass ratio, and thus the geometry of the system (see, e.g., Barai et al. 2004). For this reason, radial velocities of the primary were measured from the high-resolution *IUE* spectra.

First, we calculated the synthetic spectrum of the primary with the SYNSPEC code (Hubeny et al. 1994). Once again, Kurucz models and line lists, with vacuum wavelengths, were used (Kurucz 1993a, 1993b). Since the observed ultraviolet lines were narrower than expected from the rotational velocity ($v \sin i = 168$ km s^{-1}; Table 6), the synthetic spectrum was convolved with a rotation profile of 80 km s^{-1}, to improve the accuracy of the cross-correlation procedure. (Note that the slightly lower rotational velocity is consistent with our later suggestion [§ 4.2] of a circumstellar origin for the UV lines.) The radial velocities were then obtained via cross-correlation of the observed and synthetic spectra. These velocities are listed in Table 3 and displayed in Figure 8. Qualitatively, except at phase 0.25, the ultraviolet spectrum moves in phase with the primary star. However, quantitatively this trend does not overlap with the expected motion of the primary. Plavec (1988) suggested that the UV lines did not originate from the primary star but from the accretion disk. We confirm that they arise from a loosely bound, cooler structure with noncircular velocities, like an elliptical accretion disk around the primary star.

Figure 8 can also be used to speculate on the geometry and dynamics of the disk. Starting at $\phi = 0.9$, we observe the highest radial velocities corresponding to the highest infall velocities of about 40 km s^{-1}, which suggests that the streamlines in the disk are not fully circular but are influenced by the infalling gas stream. This infalling velocity component decreases as we move back in phase and disappears somewhere in the region of $\phi = 0.5$–0.6. This indicates that the streamlines are almost tangential at these phases and that the disk shape may be elliptical, with periastron at $\phi = 0.5$–0.6. At earlier phases, $\phi \sim 0.4$, we observe velocities more negative than expected, which indicates outflowing streamlines in agreement with the elliptical disk model. The only measurement that does not concur with this model is the one at $\phi = 0.25$, which was obtained during the same epoch (3363; Table 2) as several other points in Figure 8.

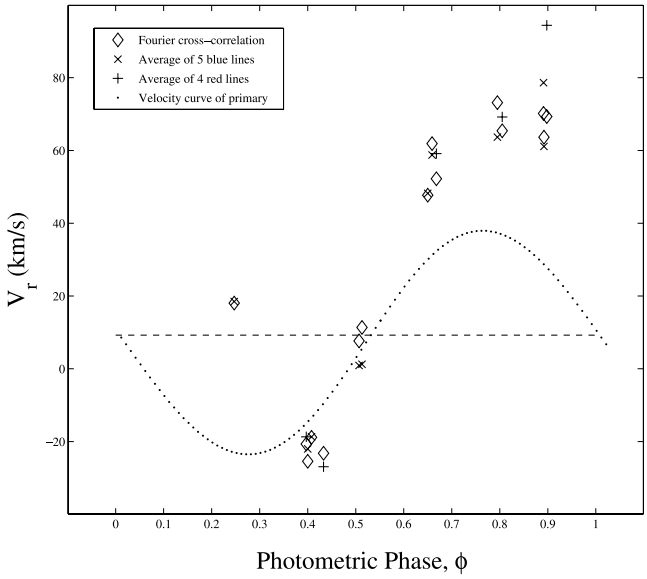

FIG. 8.—Radial velocities of UV lines compared with the velocity curve of the primary star (*dotted line*). The deviation from this curve suggests that the measured UV lines do not originate from the primary but from a loosely bound structure with noncircular velocities, like an asymmetric or elliptical disk around the primary star. [*See the electronic edition of the Journal for a color version of this figure.*]

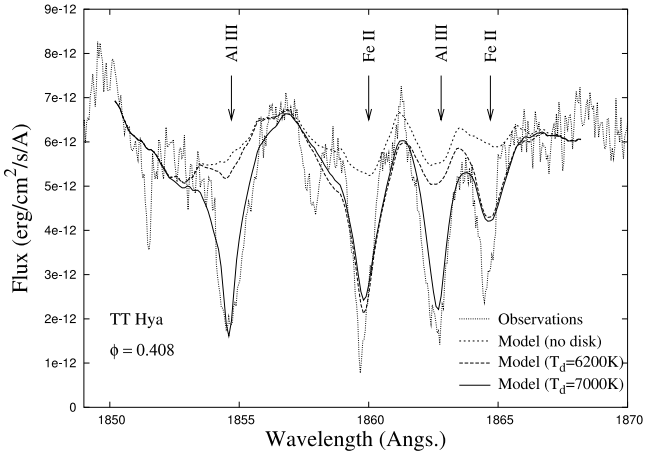

FIG. 9.—Observed and synthetic ultraviolet spectra in absolute flux units in the vicinity of the Al III resonance lines. Calculations demonstrate that the UV absorption lines seen outside of the eclipses do not originate from the primary star but mainly from the accretion disk, which has a characteristic temperature, $T_d \sim$ 7000 K. [*See the electronic edition of the Journal for a color version of this figure.*]

4.2. *Synthetic and Observed Iron Curtain Spectra outside of the Eclipses*

The ultraviolet spectrum of an Algol-type binary is dominated by the light of the primary star (except during total primary eclipse) since the contribution from the cooler secondary star is insignificant at these wavelengths. The UV region in TT Hya contains many absorption-dominated spectral lines. However, these lines do not originate from the primary star but probably from an accretion disk as suggested by Plavec (1988) based on their narrow widths and unusual depths.

Most of the lines in the UV spectrum are blended Fe II lines, which are often referred to as the "iron curtain" (Shore 1992). The "iron curtain" origin of the UV lines is confirmed by their radial velocities (see § 4.1), which are decoupled from the velocities of the primary star. These sharp and deep absorption lines were used to derive an independent estimate of the temperature of the accretion disk. We modeled the region of the UV spectrum in the vicinity of the Al III λ1854 resonance doublet from 1850 to 1867 Å. The following nine spectral lines were used to derive the final model: Fe II λ1854.659, Al III λ1854.716, Fe II λ1859.746, Fe II λ1860.053, Fe II λ1860.132, Al II λ1862.478, Al III λ1862.790, Fe II λ1864.647, and Fe II λ1864.749.

As in the case of the optical spectra, the synthetic spectrum of the primary star was calculated using the SYNSPEC code (Hubeny et al. 1994). Solar abundances, Kurucz models and line lists with vacuum wavelengths (Kurucz 1993a, 1993b), and a microturbulence of 2 km s^{-1} were assumed. This spectrum was then assigned to the star, and a complex spectrum of the star and disk in absolute units was calculated with the SHELLSPEC code (Budaj & Richards 2004). The geometries of the primary star and disk were taken from BRM05, and our derived distance of 203 pc was assumed in the calculations. The density of the disk was also adopted from BRM05 since these values were obtained from the Hα emission strength, which provides a good measure of the density. The electron number density was derived using the Newton-Raphson linearization and iteration method from the temperature, density, and abundances. The initial temperature of the primary star ($T_{\rm eff} = 9900$ K) was previously derived from the UV continuum by Plavec (1988). However, the temperatures of the star and disk were varied to match the observed *IUE* spectra.

The best fit to the local continuum was obtained from the Kurucz models for a stellar temperature $T_{\rm eff} = 10{,}000$ K, which is in very good agreement with the result of Plavec (1988). The Al III and Fe II lines in this region are sensitive temperature indicators, and a disk temperature of $T = 7000$ K provided the best fit to the UV lines. At cooler temperatures, the Al III lines in the synthetic spectra disappear, while hotter temperatures lead to a disappearance of the Fe II lines in the synthetic spectra. This new disk temperature is in good agreement with the estimate of $T = 6200$ K found by BRM05 from the Hα line. In addition, the new disk temperature is $\sim\frac{2}{3}T_{\rm eff}$ of the primary star, which is a common assumption in the case of Be star disks (Hummel & Vrancken 2000; van Kerkwijk et al. 1995) and may indicate that the Be disk phenomenon may extend to the Algol-type binaries.

Thomson scattering in the disk does not affect the spectrum significantly since the disk is optically thin in the continuum. In the center of strong lines, like the Al III λ1854.7 line, the opacity can be 3–4 orders of magnitude higher than in the continuum and the optical depth can sometimes be greater than 10. Under these circumstances, the assumption of an optically thin medium in the treatment of scattering is not fulfilled within the SHELLSPEC code. However, in LTE, the line-source function is the Planck function; thus, the scattering does not affect the lines at all. Table 6 summarizes the parameters of the star and disk derived from this UV region.

Figure 9 clearly demonstrates that the synthetic stellar spectrum of the primary cannot fit the UV absorption lines. Once the disk is included, a disk temperature of $T = 7000$ K provides a better fit to the observed Al III lines than a temperature of $T = 6200$ K.

4.3. *Synthetic and Observed UV Spectra during Total Eclipse*

A total eclipse of the primary star provides a unique opportunity to study the energy balance between the stars and circumstellar matter, the effects of various radiative processes, and the geometry of the circumstellar material. For this reason, we used

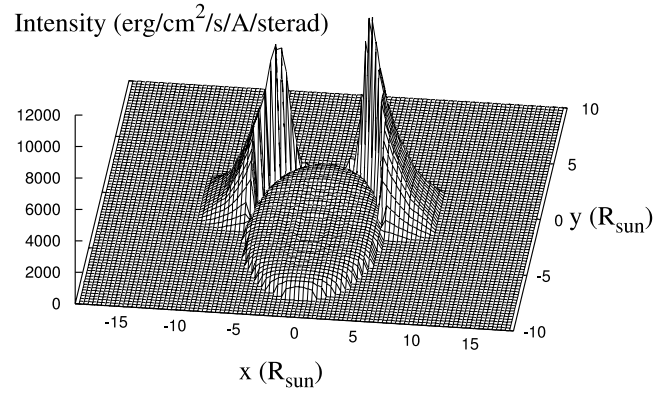

FIG. 10.—Two-dimensional projection image of TT Hya in the continuum near 1850 Å during total eclipse ($\phi = 0.001$). The central rounded structure represents the image of the secondary star. Its rounded shape results from limb darkening, while the depression in the center of the secondary star is due to the gravity darkening. The large peaks on either side of the secondary star represent the disk emission, which is mainly due to Thomson scattering of the light from the primary star. The primary star is hidden behind the image of the secondary.

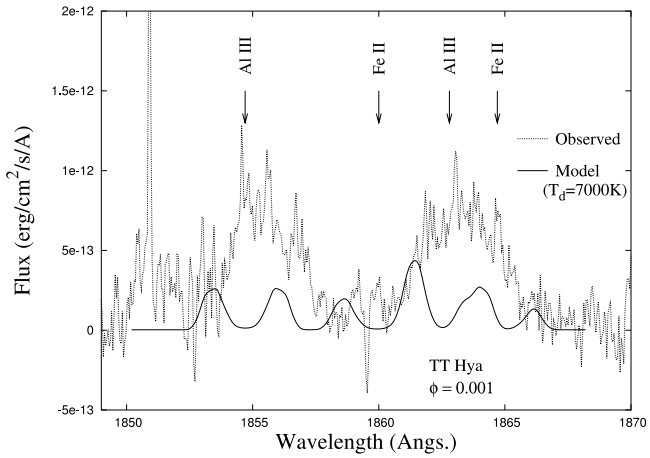

FIG. 11.—Short-wavelength region of the *IUE* SWP high-resolution spectra of TT Hya during total eclipse (*dotted line*) compared with the synthetic spectrum (*solid line*), which includes both stars and the disk (disk temperature $T_d = 7000$ K). It is clear that the disk cannot account for the emission lines of higher ions. [*See the electronic edition of the Journal for a color version of this figure.*]

SHELLSPEC to calculate the total absolute flux in the continuum and lines during total eclipse (at $\phi = 0.001$) in the spectral region containing the Al III lines (1850–1867 Å). The parameters of the disk and primary star were assumed from the previous section. However, the secondary star had to be included in the calculation of the spectra seen during total primary eclipse. In the calculation of the synthetic spectra, the secondary was considered to be a blackbody with a temperature of $T = 4600$ K at the rotation poles. Roche geometry, limb darkening, and gravity darkening were included. At $\lambda \approx 1850$ Å the model based on two stars and a disk predicts a total absolute *continuum* flux of $F_\lambda = 3\times10^{-15}$ ergs cm^{-2} s^{-1} Å^{-1}. Approximately one-half of this flux comes from scattered light in the disk arising from the primary, while thermal radiation of the disk is negligible (on the order of 1%). The continuum flux from the secondary star is comparable to that of the scattered light. Figure 10 illustrates a two-dimensional projection image of the system (as if seen on the sky) at midprimary eclipse ($\phi = 0.001$) for wavelengths near 1850 Å in the continuum. In this figure, the image of the secondary star is rounded because of limb darkening, while the depression in the center of the secondary star is due to gravity darkening. The large peaks on either side of the secondary star represent the disk emission, which is mainly due to Thomson scattering.

The fit between the observed and synthetic spectra at midprimary eclipse is illustrated in Figure 11. The lines that were seen in absorption outside of the eclipses become double-peaked emission lines during total eclipse. At lower resolution, these lines would become unresolved and should create a pseudocontinuum with a flux of $\sim F_\lambda = 1\times10^{-13}$ ergs cm^{-2} s^{-1} Å^{-1} level. This is in agreement with Plavec (1988), who determined the pseudocontinuum flux of 1.2×10^{-13} ergs cm^{-2} s^{-1} Å^{-1} from low-resolution *IUE* spectra at this wavelength. However, it is clear from Figure 11 that a disk with a temperature of $T = 7000$ K cannot account for the emission seen in lines of higher ions like Al III during primary eclipse. A hotter emission source, with geometry and dynamics different from an accretion disk, is required to explain the observed spectra. The most important opacity source in the continuum at this phase is Thomson scattering. This opacity source is typically 2 orders of magnitude higher than the hydrogen bound-free opacity, which is a few times higher than the Rayleigh scattering on neutral hydrogen, and the Rayleigh scattering is about 2–3 orders of magnitude higher than the hydrogen free-free opacity.

Lynch et al. (1996) carried out spectropolarimetric observations of TT Hya in the spectral region from 1600 to 2300 Å during total eclipse. They reported the presence of a nonstellar continuum that was considerably polarized (20%–30% at the shortest wavelength). Based on previous arguments, this continuum is a pseudocontinuum created by emission in the lines. The fact that this light is polarized indicates that the line emission is not fully thermal but that there is scattering in the lines as well. This finding suggests that the real source function in the lines is not fully a Planck function and that there are departures from LTE, which leads to non-LTE effects.

4.4. *The* Si IV, C IV, Al III, *and* Mg II *Emission Lines during Total Eclipse*

During the total eclipse of the primary star, various emission lines of highly ionized species can be identified. Plavec (1988) could not explain the source of this ionization. Figure 12 illustrates the high-resolution *IUE* spectra of the Si IV ($\lambda\lambda$1394, 1403), C IV ($\lambda\lambda$1548, 1551), Al III ($\lambda\lambda$1855, 1863), and Mg II ($\lambda\lambda$2796, 2804) doublets during primary eclipse. Each emission line has a single-peaked profile, which suggests that this emission does not originate in a disk. The line centers (except for Mg II) are redshifted by about 100–200 km s^{-1}, and the line widths extend to $\pm$300 km s^{-1} from the line centers.

Comparison with our synthetic spectra also suggests that the disk temperature ($T = 7000$ K) is too low to produce these lines. Moreover, these lines cannot originate on the primary or in the inner part of the disk since these regions are eclipsed at this phase. So, these highly ionized lines must originate from a region with considerable vertical dimension above (or below) the orbital plane. Peters & Polidan (2004) arrived at the same conclusions based on their studies of high- to moderate-ionization emission lines in the FUV obtained with the *Far Ultraviolet Spectroscopic Explorer* (*FUSE*). They suggested the presence of a bipolar jet to account for these features. However, their interpretation may not provide a sufficient explanation for the observed *IUE* spectra. Symmetric bipolar jets perpendicular to the orbital plane and with an orbital

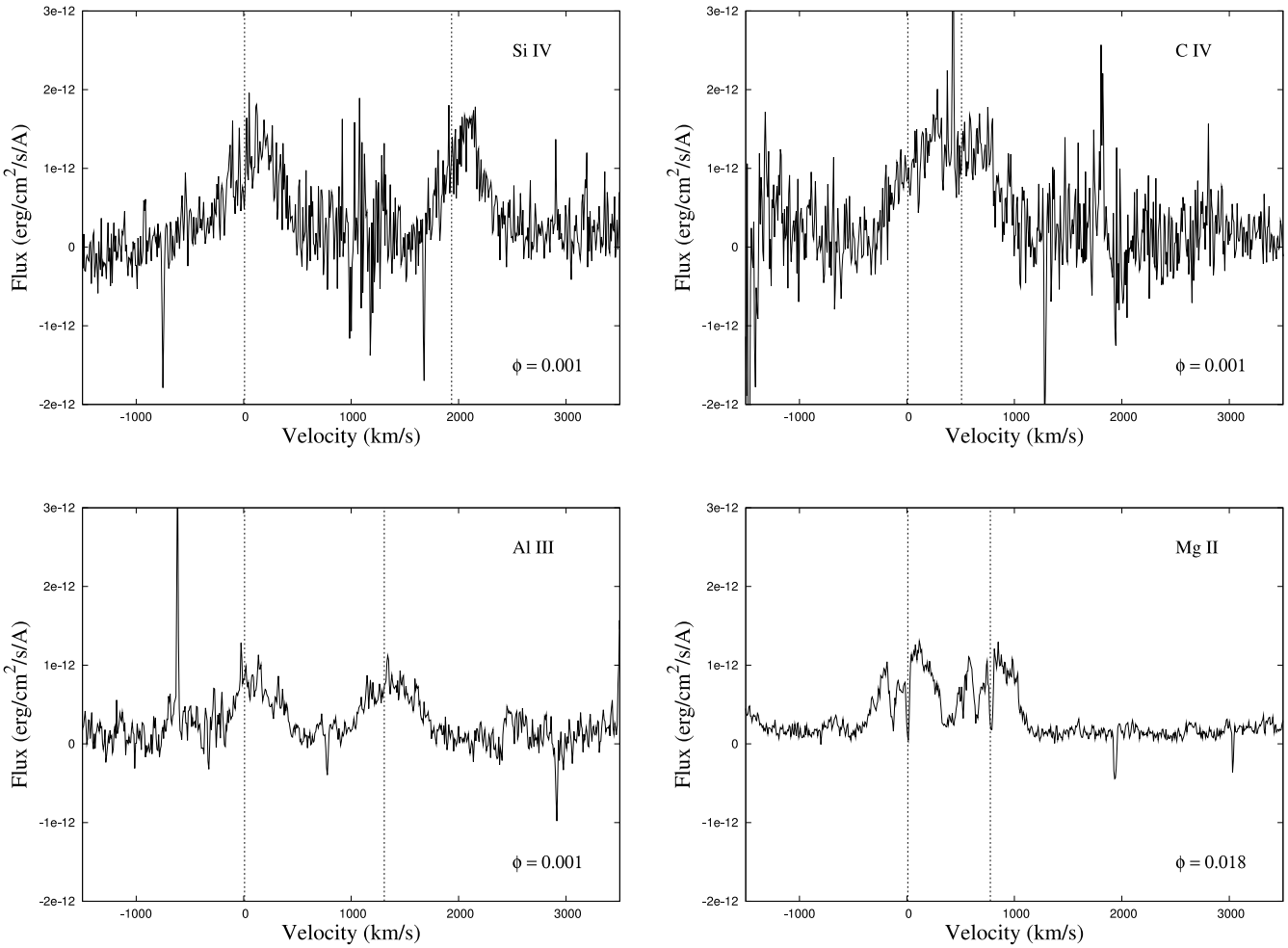

FIG. 12.—Si IV ($\lambda\lambda$1394, 1403), C IV ($\lambda\lambda$1548, 1551), Al III ($\lambda\lambda$1855, 1863), and Mg II ($\lambda\lambda$2796, 2804) doublets during the total eclipse of the primary in TT Hya. The vertical lines correspond to the wavelength in a vacuum of the doublet lines shifted to the mass center of the system. The Si IV, C IV, and Al III lines were obtained at $\phi = 0.001$, and the Mg II line at $\phi = 0.018$.

inclination of 83° would lead to jet velocities of $\sim$1200 km s^{-1}. One jet would have to be occulted during the eclipse since we observe only one redshifted feature. Thus, the jets would have to be shorter than about 7 $R_\odot$. Moreover, we should expect an occulted jet to display blueshifted emission based on geometric arguments, rather than the redshifted emission that was observed. The jets would also have to be highly collimated, with opening angles $90^\circ - i \sim 10^\circ$ to avoid smoothing the observed redshifted emission. Consequently, there are many constraints on the jet model. We propose, instead, that the emission arises from a hot disk-stream interaction region and an extended region near the impact site. This region would have a redshifted radial velocity component of the correct size during total eclipse and would naturally have higher temperatures than the disk. The structure would also extend below and above the disk plane due to the disk-stream interaction and be turbulent with supersonic velocities. The region would be unocculted near third contact, which would explain the behavior of O VI detected by Peters & Polidan (2004).

4.5. *The Lyα Line*

Another interesting feature can be observed in the new high-resolution HIRES spectra. The Lyα core is observed in emission and this emission is very sharp, with a maximum half-width of $\sim$70 km s^{-1}. Figure 13 shows that the Lyα line is relatively stable during a single epoch, independent of phase (e.g., epoch 3363; Fig. 13*a*). However, Figures 13*b* and 13*c* suggest that the Lyα emission can be highly variable. It can undergo a sudden enhancement, a small wavelength shift, or display an asymmetry as illustrated in Figure 13*b*. The spectra at epoch 3363 (Fig. 13*a*) are all very similar and slightly blueshifted relative to the center of mass of the binary, while those at epochs 2867, 2876, 3500, and 3501 are nearly identical but slightly redshifted (Figs. 13*b* and 13*c*). A flarelike event or outburst occurred between epochs 2867 and 2874 and was gone by epoch 2876, within two orbital cycles (Fig. 13*b*).

There are several possible explanations of this Lyα line behavior: (1) non-LTE effects in the atmospheres of the stars, (2) a temperature inversion in the atmospheres of the stars, (3) emission originating from extended volumes of circumstellar material, or (4) emission not originating in the binary system, but in Earth's geocorona or in our solar system. Since the line does not move according to the orbit of either star, we can reject the first two hypotheses. Since the line is very sharp, any circumstellar material would have to be very far from the stars to avoid line broadening by Keplerian motions. If the circumstellar structure is in the form of a shell, we can estimate the inner radius of this structure (the distance from center of mass of binary) to be $\geq$130 $R_\odot$ by

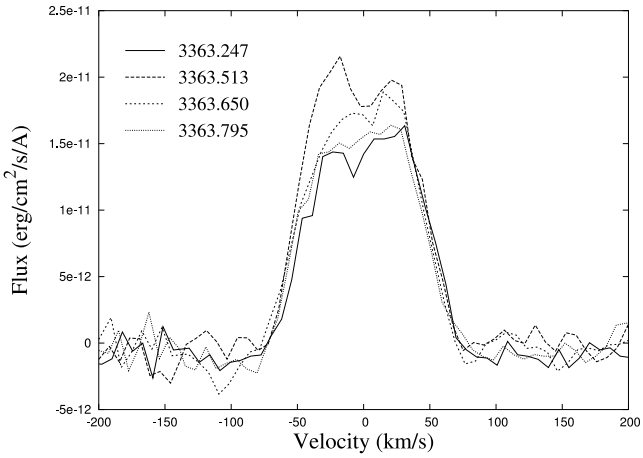

FIG. 13*a*

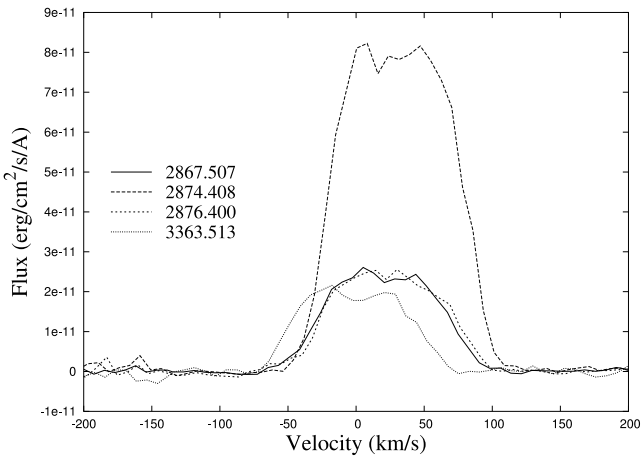

FIG. 13*b*

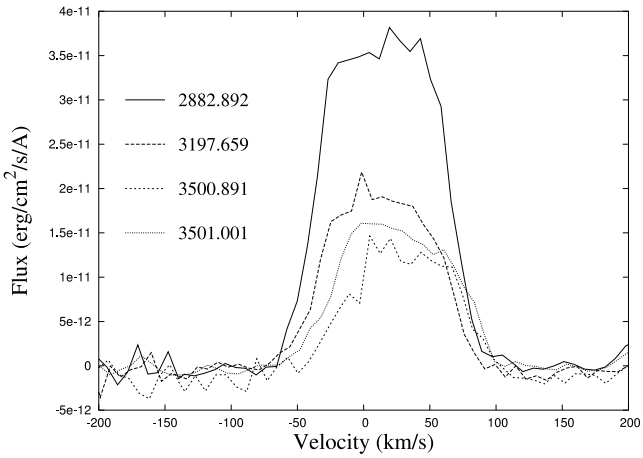

FIG. 13*c*

FIG. 13.—Lyα line of TT Hya (*a*) at different phases out of eclipse during a single epoch, (*b*) at similar phases close to secondary minimum but at different epochs, and (*c*) at different epochs and phases including total eclipse. The expected amplitude of the velocity curve of the primary star is about ± 30 km s^{-1}. The velocities are shifted to the frame of the center of mass of the system.

equating the Keplerian velocity with the maximum half-width of the line and assuming that the masses of the stars are $M_1 + M_2 = 3.40\,M_\odot$. The maximum velocities observed during the outburst event (Fig. 13*b*) were $v \leq 110$ km s^{-1} measured from the red wing of the line. Subsequently, the volume of gas involved in the outburst would have a radius of $R_{\rm max} = vt \leq 190\,R_\odot$. However, more data are needed to understand the origin of these outbursts, and hypothesis 4 provides the most likely explanation for the Lyα emission.

5. DOPPLER TOMOGRAPHY OF THE Hα SPECTRA

Doppler tomography has been a useful tool for providing images of the complex accretion structures in the Algols (see Richards 2001, 2004 and references therein). In this work we have used this technique to make images of the accretion structures in the binary, in order to examine the quality of the fits between the observed and synthetic Hα spectra, and to demonstrate the effectiveness of the SHELLSPEC code in modeling selected accretion structures. The synthetic Hα spectra used in this section were described in § 3.4 with the disk properties derived from the analysis of the UV spectra (see § 4.2 and Table 6). For these calculations, we used the newly derived mass and radius of the primary ($M = 2.77\,M_\odot$, $R = 1.99\,R_\odot$; see Table 5). The assumed disk temperature was 7000 K, and the initial gas stream temperature was 8000 K. We also calculated synthetic spectra using the values derived by Van Hamme & Wilson (1993) ($M = 2.63\,M_\odot$, $R = 1.95\,R_\odot$) and found that the two sets of synthetic spectra were nearly identical. As expected, the profiles are more sensitive to the temperature and density of the disk than to small changes in the stellar mass and radius.

The Doppler tomograms were derived from the 1985–2001 Hα data in several groups: (*a*) the observed spectra, (*b*) the observed spectra minus the synthetic stellar spectra, (*c*) the observed spectra minus the synthetic spectra of the stars and accretion disk, and (*d*) the observed spectra minus the synthetic spectra of the stars, disk, and gas stream. These images were derived for three data sets to illustrate the changes with time: (1) 1985–1991, (2) 1994–2001, and (3) the entire data set from 1985 to 2001. The reconstructed images of the Hα accretion sources are shown in Figure 14.

Row 1 of Figure 14 shows that the observed Hα emission originated from a part of the disk structure whose outer edge was close to the Roche surface of the star but whose inner edge did not touch the surface of the primary. The tomograms shown in row 2 of Figure 14 were based on the difference spectra when only the stars were included in the synthetic spectrum. They show that the accretion disk dominated the emission profile once the stellar contribution was removed from the observed spectrum. When the stars and disk were all modeled in SHELLSPEC and difference profiles were calculated, the resulting image was almost clear (Fig. 14, row 3); however, enhancement of this image showed that two structures remained: emission along the gas stream and a portion of the accretion disk (Fig. 14, row 4). Finally, when the stars, disk, and gas stream were all incorporated into the synthetic profile, the tomogram showed an almost clear image once again as in row 3 of Figure 14, but enhancement of this final image showed that the gas stream emission had disappeared, and the only structure that remained arose from the locus of the accretion disk (Fig. 14, row 5). The main difference between the 1985–1991 (*left column*) and 1994–2001 (*middle column*) data sets was that the disk emission was generally stronger during the earlier epoch than in the later epoch. In addition, the

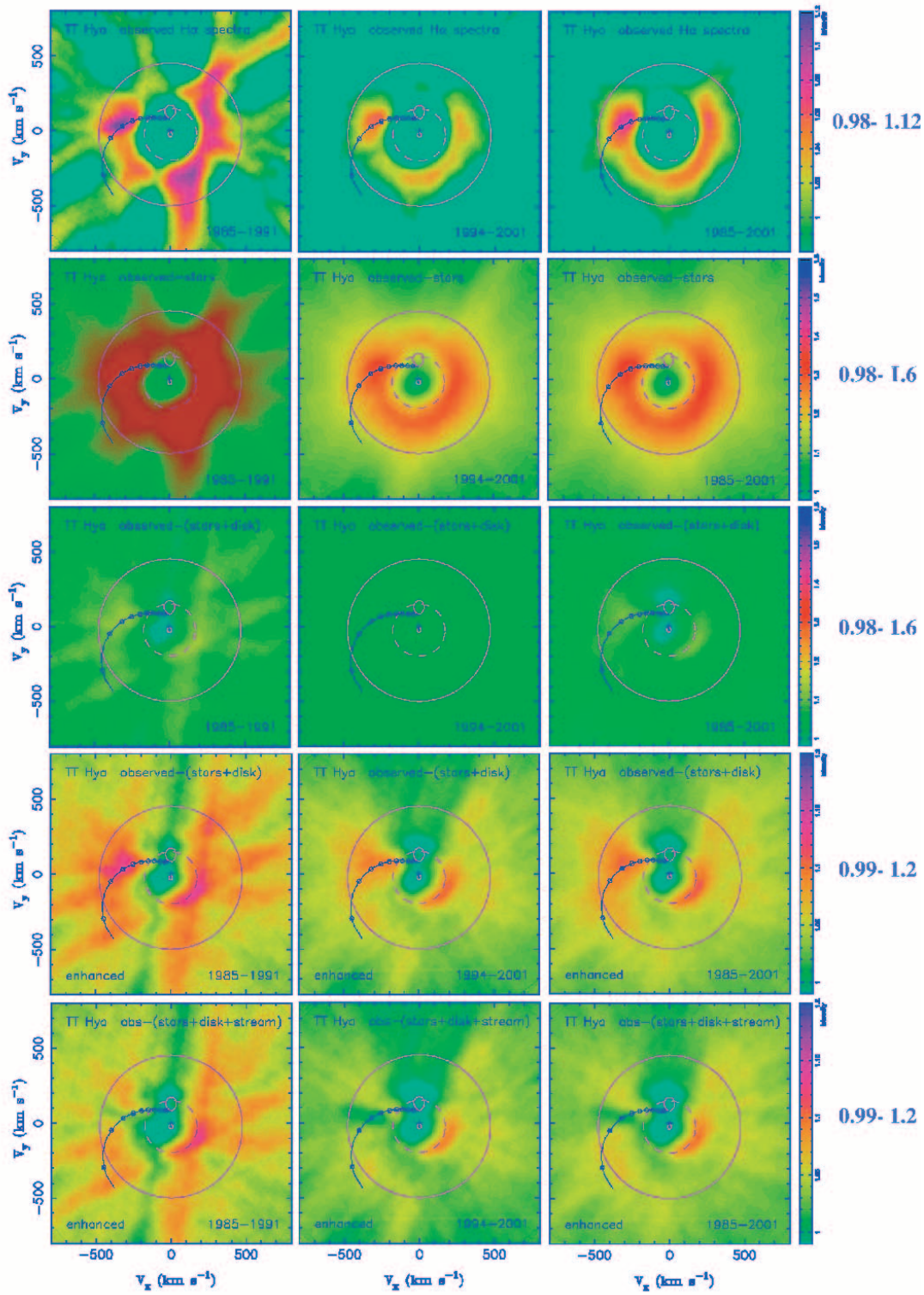

FIG. 14.—Hα Doppler tomograms of TT Hya for (1) 1985–1991 (*left column*), (2) 1994–2001 (*middle column*), and (3) all data from 1985 to 2001 (*right column*). The different rows show the observed spectra (row 1; image intensity $I = 0.98$–1.12), observed spectra minus stars (row 2; $I = 0.98$–1.6), observed spectra minus stars and disk (row 3; $I = 0.98$–1.6), enhanced version of row 3 (row 4; $I = 0.99$–1.2), and enhanced version of observed spectra minus stars, disk, and gas stream (row 5; $I = 0.99$–1.2).

phase coverage during the earlier epoch was not as good as during 1994–2001, with only a few spectra between $\phi = 0.4$ and 0.7 (Fig. 1), which explains the streaky appearance of the 1985–1991 images.

These Doppler images suggest that the SHELLSPEC code can be used to sequentially model the stars, disk, and gas stream. Only a very faint portion of the disk could not be modeled. Comparisons with simulated Hα tomograms of TT Hya based on hydrodynamic simulations by Richards & Ratliff (1998) suggested that the unmodeled region was indeed part of an asymmetric accretion disk (see Fig. 15). This region was not modeled by SHELLSPEC because the code assumes a circular Keplerian

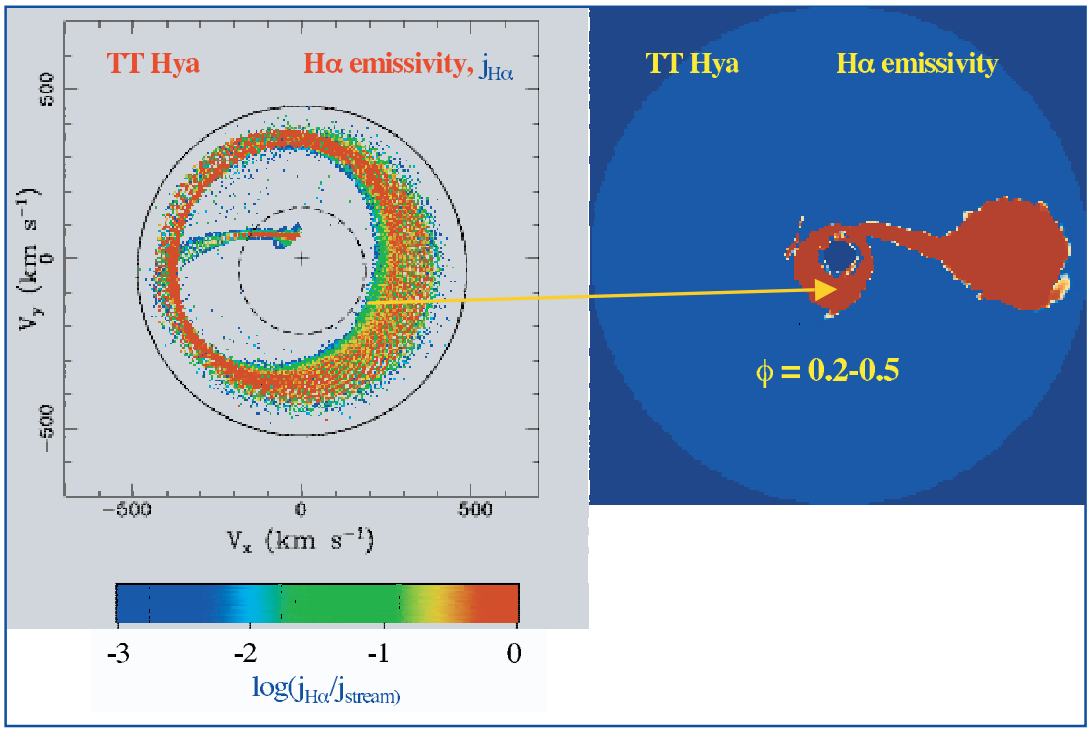

FIG. 15.—Eccentric disk in TT Hya, with asymmetry near phases 0.2–0.5, based on hydrodynamic simulations by Richards & Ratliff (1998).

disk structure. This result provides the first observational confirmation that the disk in TT Hya is elliptical and asymmetric. Moreover, the similarity between the tomogram based on the observed Hα spectra only and that based on the observed minus stellar contribution suggests that the gas in the accretion disk is optically thin at Hα, as assumed in the differencing procedure (see Richards 1993, 2004). Tomograms of another Algol binary, CX Dra, suggested that the disk in that system was not optically thin (Richards et al. 2000).

6. CONCLUSIONS

The main achievements of this work can be summarized as follows:

1. We have developed a systematic procedure to study the disks in Algol-type binaries using spectroscopic analysis, synthetic spectra, and tomography. This procedure can be used to study other Algol disk systems like TT Hya (e.g., AU Mon). With minor modifications, this approach can be used to study the disks in novae and cataclysmic variables.

2. New velocity curves and orbital parameters have been derived for TT Hya from an analysis of Hα and UV spectra. Our study has more than quadrupled the previous 27 radial velocity measurements and nearly tripled their precision.

3. The derived orbital eccentricity was found to be small, but nonzero ($e = 0.021 \pm 0.003$ based on the best photometric fit). An eccentric orbit could lead to enhanced mass transfer near and shortly after periastron, which might explain the enhanced activity of TT Hya and other Algols at these phases.

4. A lower limit of the mass transfer rate was estimated (2×10^{-10} $M_\odot$ yr^{-1}).

5. The calculations of the synthetic Hα spectra have been improved within the SHELLSPEC code compared to those of BRM05. Specifically, the electron number density is now calculated within the code from the density, temperature, and abundances. The inclusion of the gas stream and the adoption of a lower surface gravity for the primary star led to an improved match between the observed and synthetic spectra.

6. High-resolution *IUE* spectra of TT Hya outside of the eclipses were compared with synthetic spectra calculated by SHELLSPEC. We have demonstrated that the ultraviolet spectrum results from the combined contributions of the primary star and cooler surrounding disk.

7. The ultraviolet spectra were used to refine the properties of the accretion disk. A reliable disk temperature of about $T =$ 7000 K was found from comparisons between the observed and synthetic UV spectra of the Fe II and Al III lines in the iron curtain at out-of-eclipse phases.

8. Radial velocity measurements of the *IUE* spectra confirmed that they are decoupled from the radial velocity curve of the primary star. We propose that they originate from elliptical streamlines within the accretion disk.

9. The comparison between the observed and synthetic UV spectra showed that the emission lines of higher ionization species (e.g., Al III, Si IV, C IV) seen during total eclipse cannot originate in the disk. These emission lines could originate from the stream-disk interaction region.

10. The nonstellar pseudocontinuum during the total eclipse was studied and quantitatively explained by calculations of synthetic spectra. This continuum is most likely due to the thermal and scattered emission in the lines that becomes unresolved at lower resolution.

11. Doppler tomography of the observed Hα line confirmed the dominant disklike structure of the circumstellar material. Tomography of the difference spectra after subtracting the synthetic spectrum of the stars and disk revealed the presence of the gas stream. This gas stream was modeled effectively with the SHELLSPEC code once accurate disk and gas stream parameters were known.

12. The presence of an asymmetric disk was suggested by the noncircular nature of the radial velocity measurements of the UV lines and confirmed by the comparison between the Hα tomograms and simulated tomograms based on hydrodynamic simulations of Richards & Ratliff (1998).

We would like to thank Richard Wade, George Pavlov, and Alon Retter for many stimulating discussions about this work. This research was supported by a postdoctoral fellowship from Penn State University, NSF-NATO fellowship DGE-0312144, and NASA ADP grant NNG04GC48G.

REFERENCES

Albright, G. E., & Richards, M. T. 1996, ApJ, 459, L99
Barai, P., et al. 2004, ApJ, 608, 989
Budaj, J., & Richards, M. T. 2004, Contrib. Astron. Obs. Skalnate Pleso, 34, 167
Budaj, J., Richards, M. T., & Miller, B. 2005, ApJ, 623, 411 (BRM05)
Chung, S. M., Drake, J. J., Kashyap, V. L., Lin, L. W., & Ratzlaff, P. W. 2004, ApJ, 606, 1184
Eaton, J. A., & Henry, G. W. 1992, Inf. Bull. Variable Stars, 3737, 1
Etzel, P. B. 1988, AJ, 95, 1204
Etzel, P. B., Olson, E. C., & Senay, M. C. 1995, AJ, 109, 1269
Hubeny, I., Lanz, T., & Jeffery, C. S. 1994, Newsletter on Analysis of Astronomical Spectra, No. 20, ed. C. S. Jeffery (CCP7; St. Andrews: St. Andrews Univ.), 30
Hummel, W., & Vrancken, M. 2000, A&A, 359, 1075
Kondo, Y. 1987, Exploring the Universe with the *IUE* Satellite (Dordrecht: Reidel)
Korčaková, D., Kubát, J., & Kawka, A. 2005, in ASP Conf. Ser. 334, Fourteenth European Workshop on White Dwarfs (San Francisco: ASP), 403
Krtička, J. 1998, in Proc. 29th Stellar Conf., ed. J. Dušek, & M. Zejda (Brno: Nicholas Copernicus Obs. and Planetarium), 73
Kulkarni, A. G., & Abhyankar, K. D. 1980, Ap&SS, 67, 205
Kurucz, R. L. 1993a, CD-ROM 13, ATLAS 9 Stellar Atmosphere Programs and 2 km/s Grid (Cambridge: SAO)
———. 1993b, Kurucz CD-ROM 18, SYNTHE Spectrum Synthesis Programs and Line Data (Cambridge: SAO)
Lehmann, H., & Mkrtichian, D. E. 2004, A&A, 413, 293
Lynch, D. E., Polidan, R. S., Keyes, C. D., Nordsieck, K. H., & Peters, G. J. 1996, BAAS, 28, 1374
Maxted, P. F. L., & Hilditch, R. W. 1996, A&A, 311, 567
Miller, E. W., & McNamara, D. H. 1963, PASP, 75, 346
Milone, E. F., Munari, U., Marrese, P. M., Williams, M. D., Zwitter, T., Kallrath, J., & Tomov, T. 2005, A&A, 441, 605
Mkrtichian, D. E., Rodríguez, E., Olson, E. C., Kusakin, A. V., Kim, S.-L., Lehmann, H., Gamarova, A. Yu., & Kang, Y. W. 2005, in ASP Conf. Ser. 333, Tidal Evolution and Oscillations in Binary Stars (San Francisco: ASP), 197
Morbey, C. L., & Brosterhus, E. B. 1974, PASP, 86, 455
Nazarenko, V. V., Glazunova, L. V., & Shakun, L. S. 2005, Astron. Rep., 49, 284
Pavlovski, K., Burki, G., & Mimica, P. 2006, A&A, 454, 855
Perryman, M. A. C., et al. 1997, The *Hipparcos* and Tycho Catalogues (ESA SP-1200; Noordwijk: ESA)
Peters, G. J. 1989, Space Sci. Rev., 50, 9
Peters, G. J., & Polidan, R. S. 1998, ApJ, 500, L17
———. 2004, Astron. Nachr., 325, 225
Plavec, M. J. 1988, AJ, 96, 755
Plavec, M. J., & Polidan, R. S. 1976, in IAU Symp. 73, Structure and Evolution of Close Binary Systems, ed. P. Eggleton, S. Mitton, & J. Whelan (Dordrecht: Reidel), 289
Popper, D. M. 1989, ApJS, 71, 595
Retter, A., Richards, M. T., & Wu, K. 2005, ApJ, 621, 417
Richards, M. T. 1990, ApJ, 350, 372
———. 1993, ApJS, 86, 255
———. 2001, in Astrotomography, ed. H. M. J. Boffin, D. Steeghs, & J. Cuypers (Berlin: Springer), 276
———. 2004, Astron. Nachr., 325, 229
Richards, M. T., & Albright, G. E. 1999, ApJS, 123, 537
Richards, M. T., Koubský, P., Šimon, V., Peters, G. J., Hirata, R., Skoda, P., & Masuda, S. 2000, ApJ, 531, 1003
Richards, M. T., & Ratliff, M. A. 1998, ApJ, 493, 326
Sahade, J., & Cesco, C. U. 1946, ApJ, 103, 71
Shore, S. N. 1992, in ASP Conf. Ser. 22, Nonisotropic and Variable Outflows from Stars, ed. L. Drissen, C. Leitherer, & A. Nota (San Francisco: ASP), 342
Vesper, D., Honeycutt, K., & Hunt, T. 2001, AJ, 121, 2723
Van Hamme, W., & Wilson, R. E. 1993, MNRAS, 262, 220
van Kerkwijk, M. H., Waters, L. B. M. F., & Marlborough, J. M. 1995, A&A, 300, 259
Vivekananda Rao, P., & Sarma, M. B. K. 1994, Bull. Astron. Soc. India, 22, 451
Wilson, R. E., & Devinney, E. J. 1971, ApJ, 166, 605